LAPPEENRANTA UNIVERSITY OF TECHNOLOGY
School of Technology
Technical Physics

Evgenii Zhukov

MAGNETIZATION STUDIES OF POLYSTYRENE/MULTIWALL CARBON NANOTUBE COMPOSITE FILMS

Examiners: Professor Erkki Lähderanta
D.Sc. Ivan Zakharchuk

Abstract

Lappeenranta University of Technology
School of Technology
Technical Physics
Evgenii Zhukov

MAGNETIZATION STUDIES OF POLYSTYRENE/MULTIWALL CARBON NANOTUBE COMPOSITE FILMS

Master's thesis
2015
55 pages, 41 pictures, 9 Tables.
Examiners: Professor Erkki Lähderanta
D.Sc. Ivan Zakharchuk
Keywords: polystyrene, multi-walled carbon nanotubes, MWCNT, composite, magnetization, SQUID.

In this thesis magnetic properties of polystyrene/multiwall carbon nanotube (MWCNT) composites are investigated with Quantum Design SQUID magnetometer (MPMS XL). The surface of the composite films is studied via BRUKER Multimode 8 Atomic Force Microscope, as well. The polystyrene/MWCNT composites have been prepared by the group of professor Okotrub (Physics Chemistry of Nanomaterials laboratory, Nikolaev Institute of Inorganic Chemistry, Russia). The composite films have been prepared by solution processing and stretching method. The approximate length and inner diameter of the MWCNTs used in fabrication are 260 μm and 10 nm, respectively. The content of MWCNTs is 1 and 2.5 contents percent (wt%) for studied samples. The stretching of the samples is 30% for samples with 1 and 2.5 wt% content, and one sample with 1 wt% loading of MWCNTs is 100% stretched. MWCNTs aligned perpendicular to a silicon substrate are used as a reference sample. The magnetization field dependencies of the samples exhibit hysteresis behavior. The values of saturation magnetization of composite films are much less compared to that of the reference sample. The saturation magnetization coercitivity field value drops with decrease of MWCNT content. At high magnetic fields strong presence of diamagnetism is observed. Measurements in magnetic field parallel and perpendicular to the composite plate display anisotropy with respect to the direction of stretching. Temperature dependences of magnetization for all samples display difference between zero-field cooled and field-cooled curves of magnetization. This divergence

confirms the presence of magnetic interactions in the material. The atomic force microscopy study of the composites' surfaces revealed that they are relatively smooth and the nanotubes are aligned with the axis of stretching to some extent.

Acknowledgements

I would like to thank my supervisor, Zakharchuk Ivan, for invaluable help in process of measurement on SQUID magnetometer, detailed acquaintance with all devices in laboratory, help in checking and editing of master thesis project. I would like to thank Professor Erkki Lahderanta for advices in choosing of scientific articles, checking and estimating of my work. Also I thank a lot my parents which support me every time and give wise advices.

Lappeenranta, May 2015

Evgenii Zhukov

Table of contents

List of symbols and abbreviations

CNT – carbon nanotube

MWCNT – multi-walled carbon nanotube

SWCNT – single-walled carbon nanotube

PMMA – polymethylmethacrylate

MPMS – magnetic property measurement system

AFM – atomic force microscopy

SEM –scanning electron microscopy

FC – field cooling

ZFC – zero-field cooling

CCVD – catalytic chemical vapor deposition

Introduction

Nowadays for some electromagnetic applications polymer composites containing conductive inclusions are very promising. The most interesting matters for such application are materials which have a predetermined arrangement of the inclusions and in certain frequency range provide the electromagnetic response. Thus special attention was attracted by carbon nanotubes (CNTs), conductive quasi-one-dimensional nanoparticles because of their extremely high shielding efficiency of composites in gigahertz [1–6] and terahertz [7–11] ranges also with low nanotube concentration. Also concentration and distribution of nanotubes in matrix, the polymer nature and geometry of CNTs are properties which control the electromagnetic characteristics of CNT-based composites. Properties of a composite material could be radically changed by correction of any parameter mentioned above. For instance, reduction of dielectric permittivity, dc conductivity and electromagnetic interference shielding efficiency of composites could be made by decreasing of the defect-free-length in CNT walls [2]. The strong decreasing of sample transmission with decrease of CNT diameter was detected by microwave probing of polymethylmethacrylate (PMMA) composite with CNTs [12]. Composite properties depend also on dispersion and distribution of CNTs in polymer matrix [13]. There are few methods for filling of polymers with CNTs, for instance, spins coating [14], stretching [1,15], and forge-rolling [9,10,16]. Stretching and forge-rolling leads to alignment of nanotubes in polymer matrix and as a result in anisotropic electromagnetic properties of composites [1,2,9,10,16]. However, production of CNTs in different synthetic conditions makes impossible comparison of measurement results. Furthermore, despite that every method of nanotube production has own advantages and limitations, never was studied comparatively the properties of anisotropic composites containing the same CNT amount produced by different methods [17]. The present work is devoted to investigate the magnetic properties of CNT/polystyrene composites prepared using the nanotubes prepared by catalytic chemical vapor deposition method. For composite fabrication stretching of soft CNT/polystyrene film method was used. The measurements were done with different types of temperature and different order of samples in magnetic field. After carbon nanofibers and nanotubes innovation the chance to improve few areas in material science and a real segment of nanotechnology has showed up. A standout amongst the most critical improvement issue of utilization is value accessibility. However for nanotubes there are many potential applications in different domains.

Many amazing structures can be formed by elemental carbon in the sp^2 hybridization. Carbon can build not only well-known graphite, but also closed and open cages with honeycomb atomic

structure. The C60 molecule by Kroto [18] was the first such structure to be discovered. In spite of the fact that various carbon cages were already studied, only in 1991 the first time tubular carbon structures were observed by Iijima [19]. First were obtained the nanotubes consisting of up to several tens of graphitic shells (so-called multi-walled carbon nanotubes). Such nanotubes have adjacent shell separation of ~0.34 nm, diameters of ~1 nm and high length/diameter ratio. Only after two years single-walled carbon nanotubes (SWCNT) were synthesized by, Iijima and Ichihashi [20] and Bethune et (Figure 1).

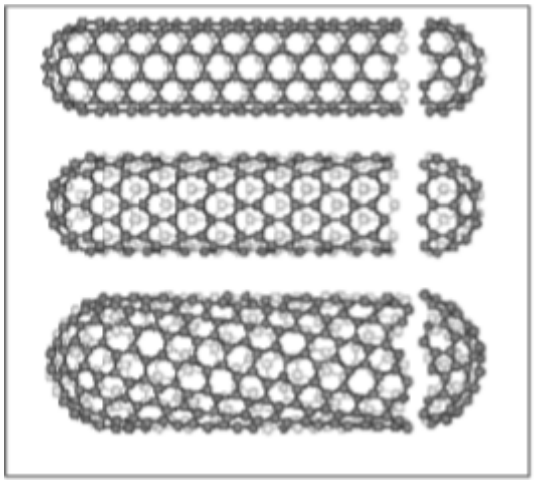

Figure 1. Single wall carbon nanotubes [21].

Only two types of nanotubes have high structural perfection. Single-walled carbon nanotubes (SWCNT) consist of a single graphite sheet seamlessly wrapped into a cylindrical tube. Multi-walled nanotubes (MWCNT) comprise an array of such nanotubes that are concentrically nested like rings of a tree trunk (Figure 2).

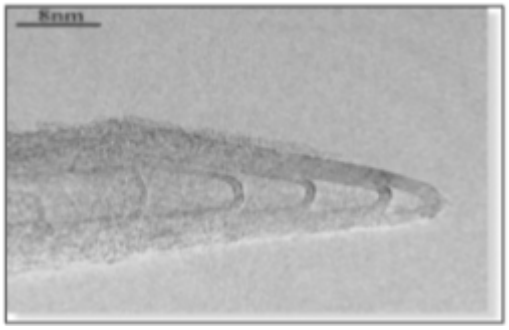

Figure 2. Tip of multi wall carbon nanotub [21].

1 Nanotubes structures

Armchair, zigzag, and chiral are three types of nanotubes which are defined by chiral vector. Their properties vary from metal to semiconductor. They have different symmetry and different functions according to the way of rolling up. Their mechanical hardness is really high besides small size.

In simplest way carbon nanotube can be described as graphene sheet rolled into a cylinder. This cylinder is one-dimensional with axial symmetry. Both ends of nanotube graphene sheet have caps, which consist of six pentagons. In order to fit the long cylindrical section the caps are perfectly placed. The length of a nanotube is approximately few microns and width is about one nanometer. The unit cell determine the classification of the different symmetries of nanotubes. The unit cell could be described as a section of the carbon nanotube, which is broken down into vectors that describe the spiral symmetry of the nanotube. Nanotube structures are represented by the following parameters.

1) Chiral vector :

$$\boldsymbol{Ch} = n\boldsymbol{a1} + n\boldsymbol{a2} \equiv (n, m) \quad (1)$$

2) Translational vector:

$$\boldsymbol{T} = tl\boldsymbol{a} + t2\boldsymbol{a2} \equiv (t1, t2) \quad (2)$$

3) Chiral angle :

$$\cos\theta = (2n + m)/(2\sqrt{n^2 + m^2 + nm}) \quad (3)$$

4) Length of chiral vector :

$$L = a\sqrt{n^2 + m^2 + nm} \quad (4)$$

Where a is the lattice constant.

5) Diameter :

$$dt = L/\pi \quad (5)$$

6) Number of hexagons in the unit cell :

$$N = (2(n^2 + m^2 + nm)/dR) \quad (6)$$

7) Symmetry vector :

$$\boldsymbol{R} = p\boldsymbol{a1} + q\boldsymbol{a2} \equiv (p, q) \quad (7)$$

8) Pitch of the symmetry vector :

$$\tau = ((mp - nq)T)/N \qquad (8)$$

9) Rotation angle of the symmetry vector:

$$\psi = 2\pi/N \text{ (in radians)} \qquad (9)$$

where $t_1 = (2m + n)/dR$; $t2 = -(2n + m)/dR$; $dR = gcd(2n+m, 2m+n)$, n,m are length of chiral vector [22].

In order to more clearly understand nanotubes structure, influence of chiral vector on single walled nanotubes will be considered.

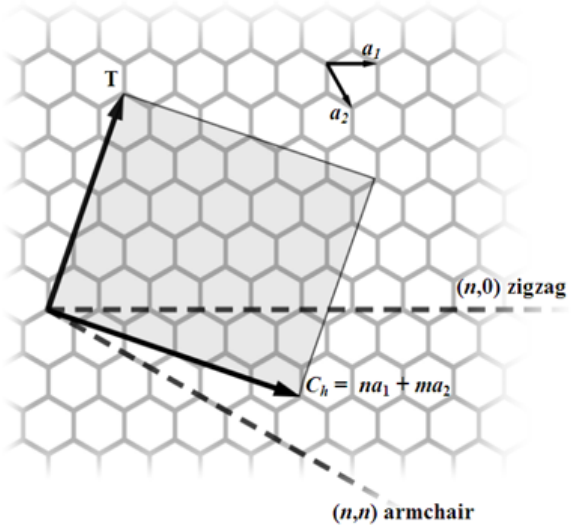

Figure 3. Types of nanotubes according to chiral vector [23].

One of the important characteristics of nanotubes is chiral vector. Different types of nanotubes could be described by the chiral vector (n, m), where n and m are integers of the vector equation $R = na_1 + ma_2$. Here a_1 and a_2 are the chiral vector is shown in the Figure 3 above. Imagine that we have one sheet of graphene. Gray square represents unrolled nanotube. In other words if one cuts this square from the whole graphene sheet and match two ends together in a cylinder one will get a nanotube. If one of the tube axis goes through hexagons center as it is shown on the picture (armchair line) such tube is armchair type. If one of the axes is parallel to zigzag line such tube is zigzag type. Changing the chiral vector from armchair line to zigzag line, one could vary nanotube properties from metallic to semiconductor. In Figure 4 is shown of zigzag and armchair nanotube structures.

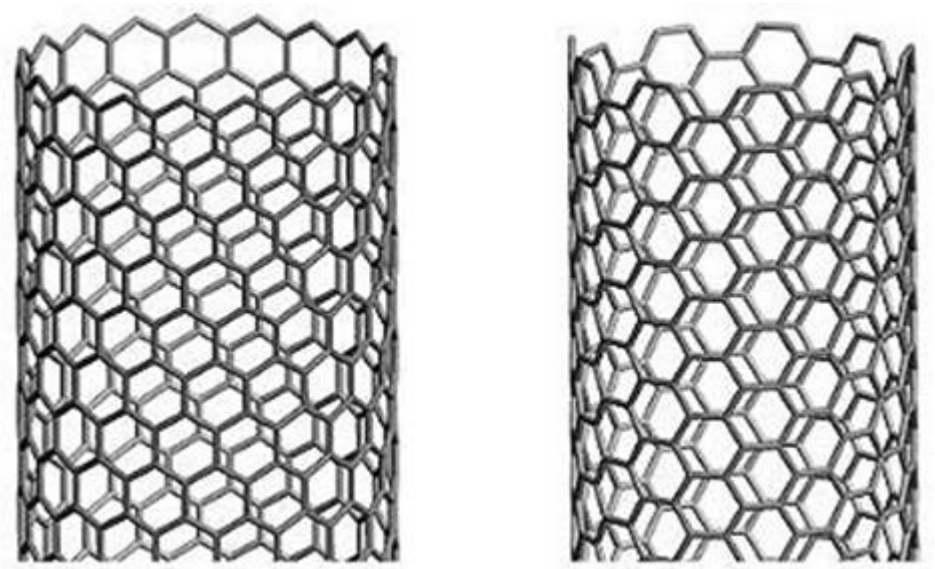

Figure 4. Examples of nanotubes. Zigzag nanotube is at left side. Armchair nanotube is at right side.

Basically, *n* and *m* define the chirality of the nanotube. The chirality determine properties of nanotubes such as conductance, density, lattice structure and other properties. If the value $n - m$ could be divided by three, then SWCNT is considered metallic. Otherwise, the nanotube is semiconducting.

The values of *n* and *m* determine the chirality, or "twist" of the nanotube. The chirality in turn affects the conductance of the nanotube, its density, its lattice structure, and other properties.

If the chiral vector is known, the diameter of a nanotube can be defined as

$$d = (n^2 + m^2 + nm)^{1/2}\ 0.0783\ nm \text{ [24].} \qquad (10)$$

1.1 CNT arm chair type

An achiral nanotube is the symmetrical classification of an armchair nanotube. The nanotube is called chiral if ti has structure that is a mirror image of the original one. When nanotube has a chiral vector where $n=m$, therefor Ch= (n, n) it is called an armchair nanotube. The chiral angel θ is equal to 30˚. For instance, when Ch= (4, 4) the chiral angle is equal to 30˚ and such nanotube is an armchair. The calculated parameters for armchair type carbon nanotube are shown in Table 1. The armchair type [4,4] and [10,10] carbon nanotube is represented on Figure 5. This figure was made in Courtesy Nano tube modeler [22].

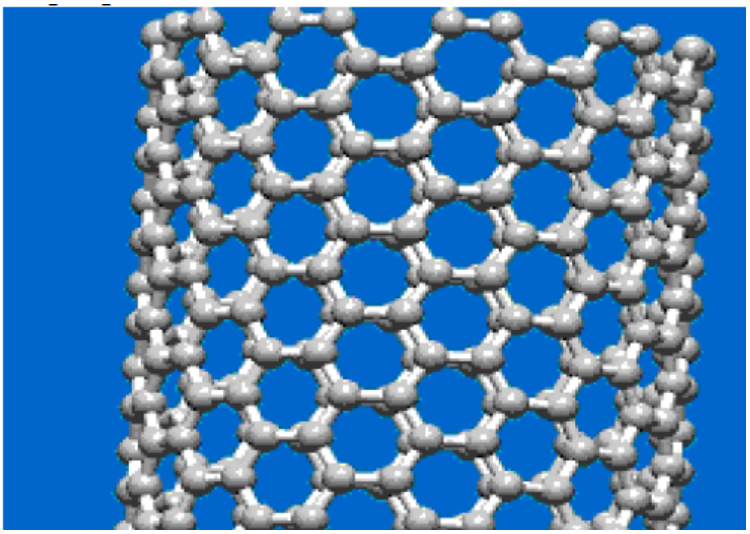

Figure 5a. SCWNT of chiral vector (10,10) of bond length 1.41 Å and tube length 20 Å. Courtesy Nano tube modeler at jcrystal.com.

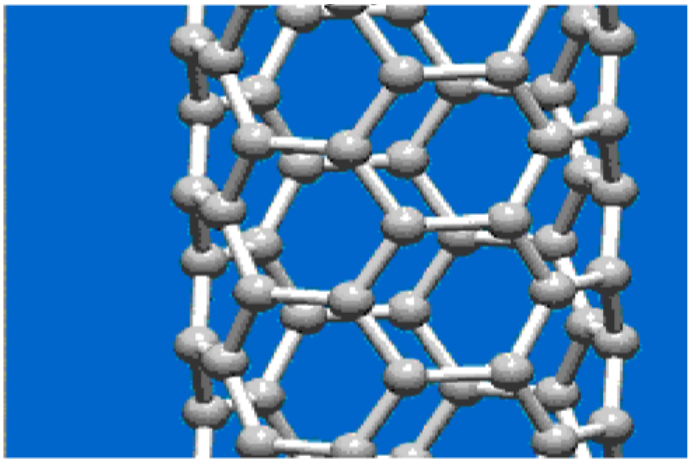

Figure 5b. SWCNT of chiral vector (4,4) of bond length 1.41 Å and tube length 20 Å. Courtesy Nano tube modeler at jcrystal.com.

Table 1. Arm chair type Carbon nano tube structure parameters calculated using nanotube modeler with length of the tube 25 Å and bond length 1.43 Å

Sample number	Chiral vector	Chiral angle	Translational vector (degrees)	Length of chiral vector (Å)	Diameter (Å)	N_o of Hexagons in unit cell	N_o of atoms in CNT	N_o of bonds used in CNT
1	4,4	30^0	1, -1	9.9	3.152866	8	136	196
2	5,5	30^0	1, -1	12.38	12.38	10	175	245
3	6,6	30^0	1, -1	14.85	4.729299	12	204	294
4	7,7	30^0	1, -1	17.33	5.519108	14	238	343
5	8,8	30^0	1, -1	19.8	6.305732	16	272	392
6	9,9	30^0	1, -1	22.28	7.095541	18	306	441
7	10,10	30^0	1, -1	24.76	7.88535	20	340	490
8	11,11	30^0	1, -1	27.23	8.658188	22	462	671
9	12,12	30^0	1, -1	29.71	9.461783	24	504	732
10	13,13	30^0	1, -1	32.18	10.24841	26	546	793
11	14,14	30^0	1, -1	34.66	11.03822	28	588	854
12	15,15	30^0	1, -1	37.14	11.82803	30	630	915
13	16,16	30^0	1, -1	39.61	12.61465	32	672	976
14	17,17	30^0	1, -1	42.09	13.40446	34	714	1037
15	18,18	30^0	1, -1	44.56	14.19108	36	756	1098
16	19,19	30^0	1, -1	47.044	14.98217	38	798	1159
17	20,20	30^0	1, -1	49.52	15.7707	40	840	1220
18	21,21	30^0	1, -1	51.99	16.55732	42	882	1281
19	22,22	30^0	1, -1	54.47	17.34713	44	928	1342
20	23,23	30^0	1, -1	56.94	1.813376	46	966	1403
21	24,24	30^0	1, -1	59.42	18.92357	48	1008	1464

1.2 CNT zig zag type

The symmetrical classification of also zigzag nanotube is classified an achiral like armchair nanotube. If nanotube structure that is a mirror image of the original one it calls achiral. This is shown in Figure 6. The chiral vector of a zigzag nanotube is vector where m=0, therefore Ch = (n, 0). The chiral angle θ is equal to 0˚. For instance, when the chiral angle is equal 0˚ the nanotube is zigzag if Ch = (10, 0). Table 2 gives the calculation of listed parameters for zigzag carbon nanotubes. This Table can be used to verify the formula mentioned above. The zigzag type nanotube with chiral vector (10,0) and chiral angle equals to 0˚ are represented in Figure 6 [22].

Table 2. Zigzag type of Carbon nano tube structure parameters calculated using nanotube modeler with length of the tube 25 Å and bond length 1.43 Å

Sample number	Chiral vector	Chiral angle (degrees)	Translational vector	Length of chiral vector (nm)	Diameter (nm)	No of Hexagons in unit cell	No of atoms in CNT	NO of bonds used in CNT
1	6,0	0^0	1, -2	8.58	2.732	12	144	204
2	7,0	0^0	1, -2	10.01	3.144	14	168	238
3	8,0	0^0	1, -2	11.44	3.643	16	192	272
4	9,0	0^0	1, -2	12.87	4.098	18	216	306
5	10,0	0^0	1, -2	14.3	4.554	20	240	340
6	11,0	0^0	1, -2	15.73	5.009	22	264	374
7	12,0	0^0	1, -2	17.16	5.46	24	288	408
8	13,0	0^0	1, -2	18.59	5.92	26	312	442
9	14,0	0^0	1, -2	20.02	6.375	28	336	476
10	15,0	0^0	1, -2	21.45	6.83	30	360	510
11	16,0	0^0	1, -2	22.88	7.286	32	384	544
12	17,0	0^0	1, -2	24.31	7.74	34	408	578
13	18,0	0^0	1, -2	25.74	8.19	36	432	612
14	19,0	0^0	1, -2	27.27	8.65	38	456	646
15	20,0	0^0	1, -2	28.6	9.108	40	480	680
16	21,0	0^0	1, -2	30.03	9.56	42	504	714
17	22,0	0^0	1, -2	31.46	10.019	44	528	748

18	23,0	0^0	1, -2	32.84	10.458	46	552	782
19	24,0	0^0	1, -2	34.32	10.92	48	576	816
20	25,0	0^0	1, -2	37.75	11.38	50	600	850

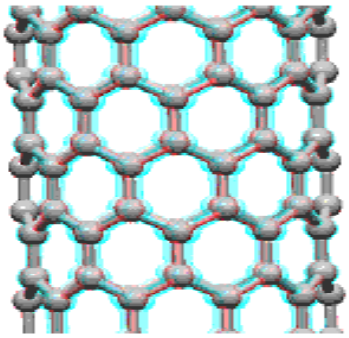

Figure 6. SWCNT with chiral vector (10,0) of bond length 1.41 Å and tube length 20 Å [22].

1.3 CNT chiral type

The symmetrical classification of a chiral nanotube is a chiral nanotube. When the nanotube has spiral symmetry which does not provide an identically structured mirror image, it is called chiral. A nanotube with chiral structure has general *n* and *m* values and Ch= (n, m). Such nanotube is represented in Figure 7. The chiral angle θ vary from 0˚ to 30˚. For instance, when Ch= (n, m) the nanotube has chiral structure and its chiral angle vary from 0˚ to 30˚. The chiral nanotube parameters mentioned above are represented in Table 3. [21]

Table 3. Zigzag type of Carbon nano tube structure parameters calculated using nanotube modeler with length of the tube 25 Å and bond length 1.43 Å

Sample number	Chiral vector	Chiral angle (degrees)	Translational vector	No of atoms in CNT	NO of bonds used in CNT
1	4,2	190	4,-5	126	182
2	10,6	21.780	11,-13	332	480
3	12,8	23.140	7,-8	412	596
4	15,12	26.320	12,-14	555	804
5	18,16	28.020	25,-26	642	1012

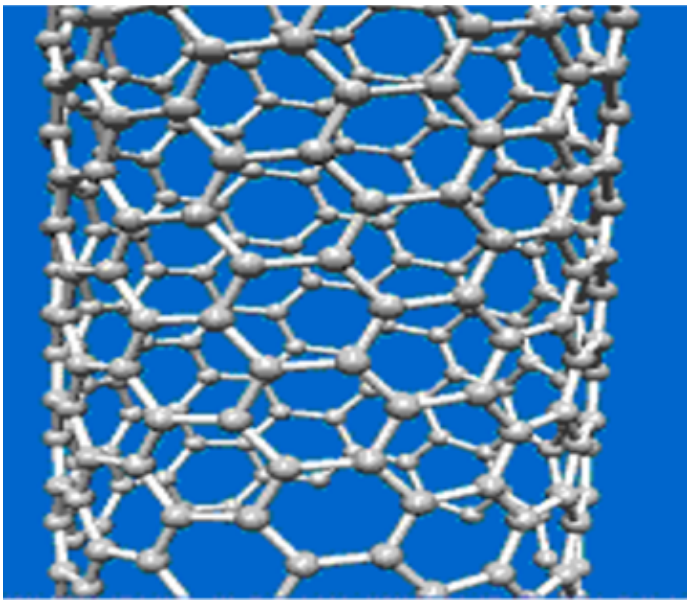

Figure 7. SWNT of chiral vector (10,6) of bond length 1.41 Å and tube length 20 Å [22].

1.4 Double-walled and Multi-walled types

Double-walled nanotube which is made in Nano explorer is represented here. The separation between inner tube and external tube is 0.34 nm. Such nanotubes are shown in Figure 8 a and b. The multi-walled carbon nanotube is represented in Figure 9 a and b [22].

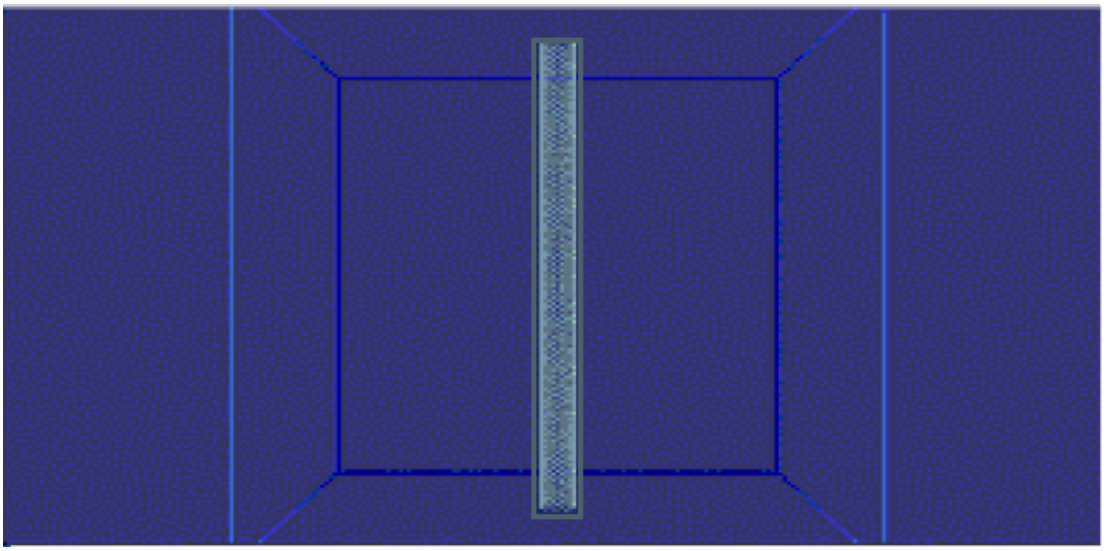

Figure 8 a. Double-walled carbon nanotube from Nano explorer tool [22].

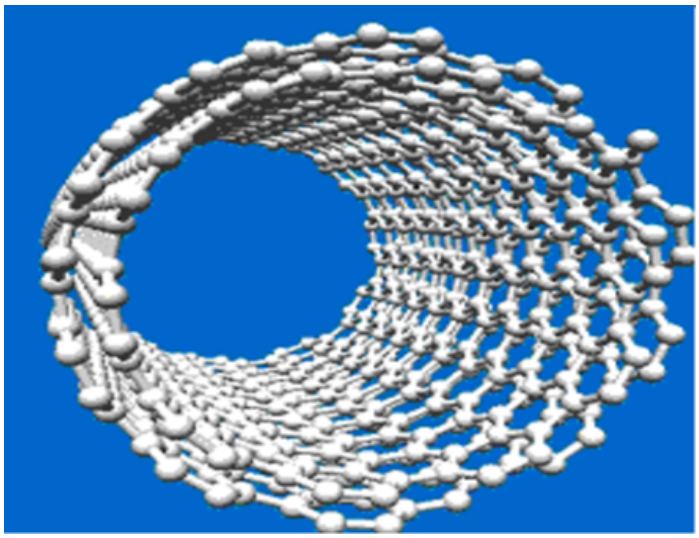

Figure 8 b. Double-walled carbon nanotube with separation of d = 0.34 nm, length of CNT is 25 Å. Number of atoms is 894, number of bonds is 1297 [22].

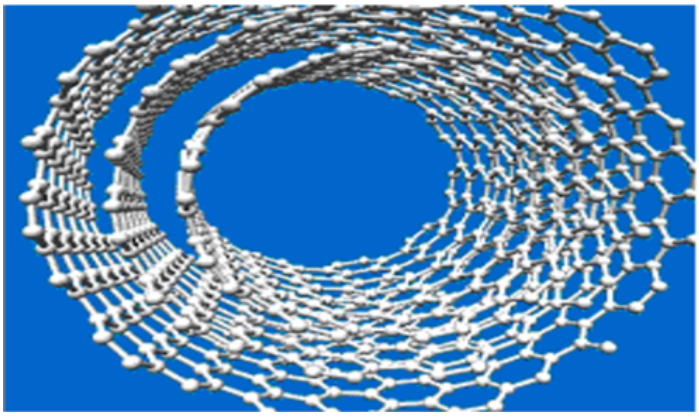

Figure 9 a. Multi-walled carbon nano tube without cap. Courtesy Nano tube modeler front View, Armchair [10,10] [22].

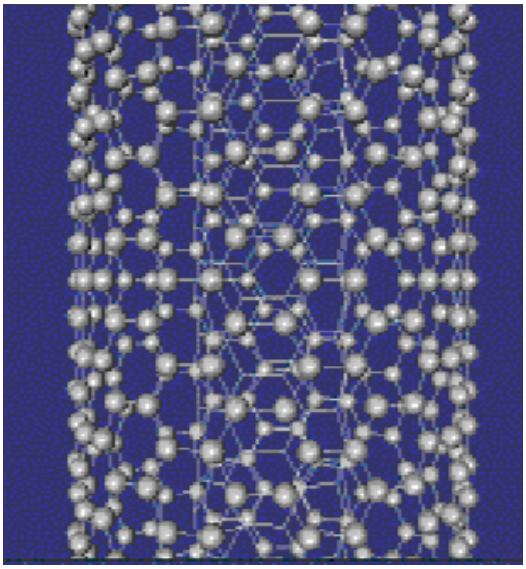

Figure 9 b. Multi-walled carbon nanotube without cap side view. Courtesy Nano explorer [22].

2 Properties of carbon nanotubes

2.1 Electrical properties

Specific structure of graphite and 1-D character are the cause of the unique electrical properties of the carbon nanotubes. The electrical resistance of the tubes is really low [25]. Due to the fact that nanotube structure is not ideal some defects could occur. Electrons which go through the tube could collide with some defects which are the cause of electrical resistance. There are several types of defects such as an impurity atom, a defect in the crystal structure, or an atom vibrating about its position in the crystal.

Because of such collision the electron could be displace from its way. Inside the carbon nanotube electrons are not easy to be scattered. In 3-D conductors, electrons have even more opportunities to be scattered. The resistance is in direct ratio to scattering that means that the increase of scattering leads to increase of resistance. As for 1-D conductor, electrons could travel forward or backward. According to these conditions only backscattering (the change in electron motion from forward to backward) could be considered as cause of electrical resistance rise. The collision which could lead to backscattering should be very strong but the possibility of such event is really low. Thus there are not so many ways for electrons to scatter. The result of such reduced scattering leads to low nanotube resistance. As a result the current which could flow through a nanotube could be really high and achieve 109 A/cm^2 [26, 27]. Because of such extraordinary property carbon nanotubes can be used as extremely good electron guns and can be used as miniature cathode ray tubes (CRTs) in thin high-brightness low-energy low-weight displays. Such displays would consist of a group of many tiny CRTs, each providing the electrons to hit the phosphor of one pixel, instead of having one giant CRT whose electrons are directed using electric and magnetic fields. If take two nanotubes with different diameters and join them in one nanotube end, to end then such nanotube could operate as diode. This suggests the possibility of constructing electronic computer circuits entirely made of nanotubes. Also nanotubes occur to be superconducting at low temperature.

2.2 Mechanical properties

As a result of the carbon sp^2 bonding [28], the carbon nanotubes have high stiffness and axial strength. The elastic response, the inelastic behavior and buckling, yield strength and fracture have to be studied for nanotubes practical application. Nanotubes have Young's modulus of 1.4 TPa which makes them the stiffest known fiber [29]. The elongation to failure could be of 20-30%, which combined with the stiffness, projects to a tensile strength well above 100 GPa

(possibly higher), by far the highest known. For comparison, the Young's modulus of high-strength steel is around 200 GPa, and its tensile strength is 1-2 GPa [30].

2.3 Thermal Properties

Diamond is one of the best thermal conductors. It was observed that carbon nanotubes have the thermal conductivity two times more than diamond [31]. CNTs have one unique thermal property. They are felt cold when they are touched, like metal, on the sides with the tube ends exposed, but similar to wood on the other side. Such difficult thermal behavior could be described primarily by phonons. The measurements give specific heat and thermal conductivity above 1 K and below room temperature. A $T^{0.62}$ behavior of the specific heat was observed below 1 K [32-37]. The linear k-vector dependence of the frequency of the longitudinal and twist acoustic phonons can explain the linear temperature dependence [38]. The transverse acoustic phonons with quadratic K dependence attribute the specific behavior of the specific heat below 1 K [39-41]. Direct information for the type of carriers and conductivity mechanisms could be obtained from the measurements of the thermoelectric power (TEP) [21].

3 Nanotubes production

3.1 Electric arc-discharge method

Electric arc-discharge method is one of the most spreaded and easiest ways to produce carbon nanotubes. Initially it was used for producing C60 fullerenes. Although it has several problems. For instance, it is a technique that produces a complex mixture of components, and requires further purification. This means that in order to get one nanotube it has to be separated from the soot and the residual catalytic metals present in the crude product. In this method two carbon rods placed end to end are used. Gap between these rods is about 1 mm. All this device is placed in inert gas atmosphere at low pressure. Also arc-discharge method can be used for producing CNTs in liquid nitrogen. Between two electrodes a high temperature discharge is created which direct current of 50 to 100A, driven by a potential difference of approximately 20 V. A small rod-shaped deposit on one electrode is formed after the discharge vaporized the surface of the other the carbon electrode. The quality of nanotubes depends on the uniformity of the plasma arc, and on the temperature of the deposit forming on the carbon electrode [42]. Figure 10 below shows schematic structure of arc-discharge method.

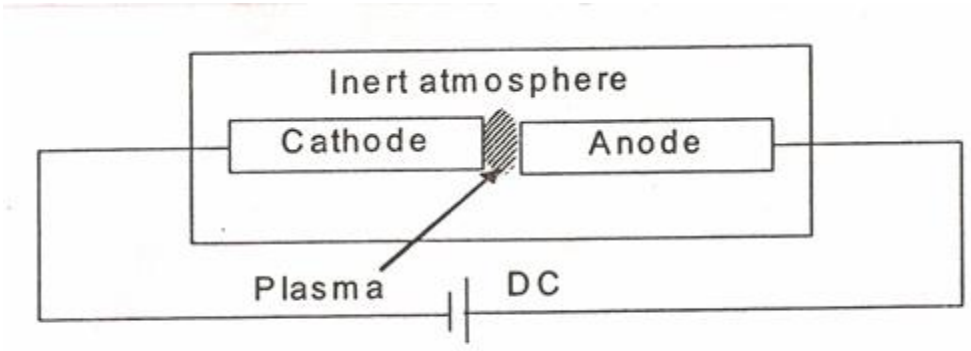

Figure 10. Schematics of arc discharge method [43].

3.2 Laser ablation method

First CNTs were synthesized using laser ablation method in 1996. A dual-pulsed laser was used and yields of >70wt% purity was achieved. Under the laser action at 1200°C in flowing argon graphite rods with a 50:50 catalyst mixture of Cobalt and Nickel started to vaporize and after followed by heat treatment in a vacuum at 1000°C the C60 and other fullerenes were removed from the obtained sample. In order to vaporize the target more uniformly, the initial laser vaporization pulse was followed by a second pulse. Due to use of two successive laser pulses the amount of soot (in this case deposited carbon) could be reduced. Laser pulse which comes second breaks up the larger particles ablated by the first one, and feeds them into the growing

nanotube structure. The material produced by this method appears as a mat of "ropes", 10-20nm in diameter and up to 100μm or more in length. The nanotubes are located in these ropes. All nanotubes in rope are single walled and aligned along a common axis. In order to vary average nanotube diameter and size distribution, the growth temperature, the catalyst composition, and other process parameters could be varied.

Arc-discharge and laser vaporization are currently the most suiTable method for small quantities high quality CNTs fabrication. Although, both methods are not without disadvantages. Firstly, these methods cannot be scaled up to industrial level because of the evaporating of the carbon source. Secondly, that vaporization methods grow CNTs in highly tangled forms, mixed with unwanted forms of carbon and/or metal species. Thus such production ways leads to the following difficulties: purifying, manipulation and assembling for building nanotube-device architectures for practical applications [42].

The Figure 11 below shows the schematic of laser ablation method.

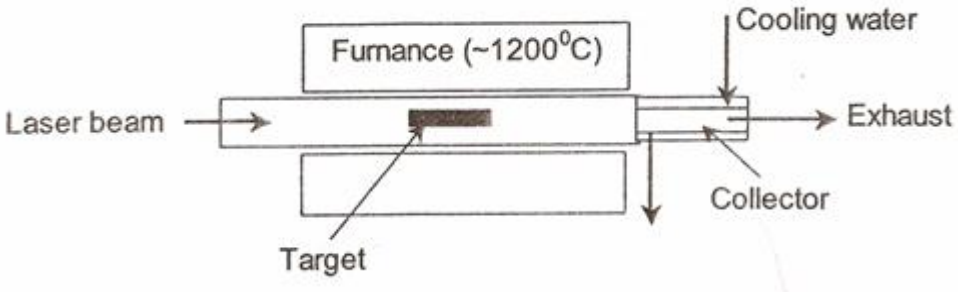

Figure 11. Schematic of laser ablation method [43].

Smalley's group at Rice University used Laser ablation or vaporization method for lab synthesis of buckyballs, single walled and multi walled (SWNT and MWNT) nanotubes. It is now being used in the industry. The type of fullerene molecule produced depends on the presence of catalyst [42].

3.3 Catalytic chemical vapor deposition (CCVD)

Over twenty years chemical vapor deposition of hydrocarbons over a metal catalyst has been used to produce various carbon materials such as carbon fibers and filaments. If the large amounts of CNTs are required it could be formed by catalytic CVD of acetylene over cobalt and iron catalysts supported on silica or zeolite. Whereas the CNTs' selectivity seems to be a function of the pH in catalyst preparation, the carbon deposition activity seems to relate to the cobalt content of the catalyst. Using the carbon/zeolite catalyst leads to fullerenes and bundles of

single walled nanotubes occurrence of which could be found among the produced mult-walled nanotubes.

In some cases CNTs could be formed from ethylene. In the ethylene atmosphere the growth of isolated single walled nanotubes or single walled nanotubes bundles seemed to be induced by supported catalysts such as iron, cobalt, and nickel, containing either a single metal or a mixture of metals. Also production of single walled nanotubes, as well as double-walled CNTs, on molybdenum and molybdenum-iron is possible. Furthermore, there is a way of usage of CVD to produce carbon within the pores of a thin alumina template with or without a nickel catalyst. The reaction temperature for the ethylene for Nickel-catalyzed CVD is 545°C, and for uncatalyzed process is 900°C. The obtained carbon nanostructure has no caps on the ends. As a carbon source also methane can be used. Mostly it was used for 'nanotube chips' production which contains isolated single walled nanotubes at controlled locations. The catalytic decomposition of a H_2/CH_4 mixture over well-dispersed metal particles such as Cobalt, Nickel, and Iron on magnesium oxide at 1000°C gave an opportunity to obtain high yields of single walled nanotubes. It has been reported that selective reduction in an H_2/CH_4 atmosphere of oxide solid solutions between a non-reducible oxide such as Al_2O_3 or $MgAl_2O_4$ and one or more transition metal oxides could be used for composite powders synthesis containing well-dispersed CNTs. At a temperature of usually >800°C a very small amount of transition metal particles could be produced by reduction. The nanoparticles growth is prevented by the decomposition of CH_4. Thus results in a very high proportion of single walled nanotubes and fewer multi-walled nanotubes [41].

In the Figure 12 is represented schematic of catalytic CVD.

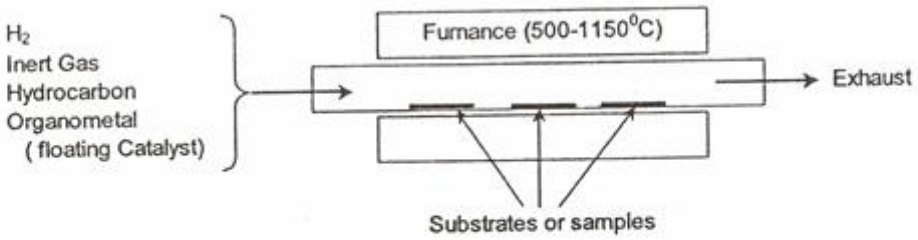

Figure 12. Schematic of catalytic CVD operated either as catalyst or substrate catalyst [43].

Chemical vapor deposition process of producing nanotubes uses a target substrate containing catalysts in a quartz tube; a hydrocarbon gas breaks apart and deposits carbon on the substrate. Through this method carbon nanotubes are produced using base growth mechanism [42].

4 Polystyrene

Polystyrene is a synthetic thermoplastic solid, hard, amorphous polymer. Polymerization product of styrene. In a large scale polystyrene is produced in the form of general purpose polystyrene and high impact polystyrene.

General purpose polystyrene is Transparent well paintable easily processable material. It is the product of polymerizing styrene in bulk or in suspension or in emulsion, and intended for the manufacture of various articles by thermoforming.

It is good dielectric, it has tensile strength of 40-50 MPa, it is resistant to acids and alkalis, and has low water absorption [44].

5 Investigated samples

5.1 Composite fabrication

Silicon substrate and MWCNT were splitted. Then a toluene solution of polystyrene was mixed with required amount of sample portion for complete polymer dissolving. Then in order to improve nanotube dispersion the composite suspension was processed by ultrasonic for ~2 min using a high-power sonic tip (200 W). Obtained slush was cast onto metallic plate and dried at ambient conditions. The sample obtained after evaporation of solvent should contain nanotubes which are randomly distributed. This composite plate had thickness approximately 220 μm. Then nanotubes should be ordered in samples. For this purpose the procedure of stretching was used.

For stretching procedure the sample was heated up to (~70 °C) by a hot air gun. A microscrew setup led to stretching of the plate in half. Overall, the composites was placed under a light load and was dried at room temperature. The thickness of the stretched plates was ~180 μm. All the prepared plates had homogeneous gray color [45].

Investigation of similar composite is showed here [45]. If the influence of magnetic field on CNTs is studied the aspect ratio is a vital parameter. The length of studied nanotubes was approximately the same due to they were grown simultaneously. However, during the processing they can become shorter. Firstly, sonication effect was checked. Polystyrene matrix of isotropic composite plate was dissolved in toluene and nanotubes were extracted. Figure 13 shows typical SEM image of the sediment.

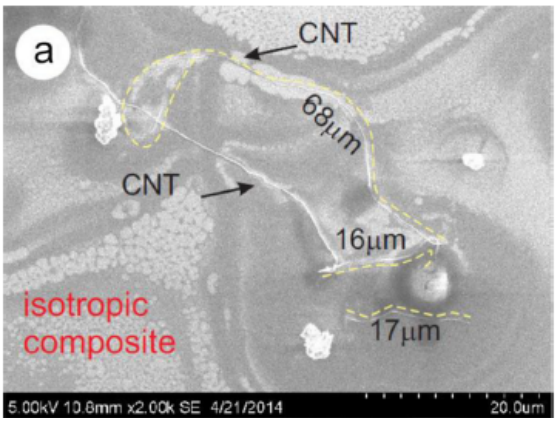

Figure 13. SEM images of MWCNT sediment extracted from isotropic composite by polystyrene dissolving. The nanotube length is indicated by numbers [45].

Good adhesion between polystyrene and CNT surface could be clearly seen from a presence of polymer in the sample. The shortening of MWCNTs down to ~50–70 μm could be determined by influence of sonication but nanotubes with a length of ~20 μm were also found. Due to the

fact that only elastic field from the polymer matrix is acted on nanotubes during stretching [46] the sonication treatment is the only cause which leads to nanotubes length shrinkage [45].

5.2 Atomic force microscopy characterization of the samples

Overall there are pictures obtained with atomic force microscopy**.** AFM measurements were done on BRUKER Multimode 8 system in MFM double pass mode with magnetic probes MFMV (made by BRUKER, USA). In first pass, Topography was measured in Tapping mode, after that same line on sample's surface was scanned again second time in Interleave mode with Lift distance to surface 100 nm. Accurate magnetic data eliminating influence from surface topography (eliminating Van der Waals forces) should be possible to be observed as magnetic structures in such scanning regime. Probe parameters were: stiffness k ~ 2.8 N/m, tip radius r ~ 40 nm and resonance frequency of scanning f = 74.59 kHz.

Scan parameters were: scan speed 0.1 Hz for scan size 10 um with resolution 512x256 pixels. No specific magnetic ordering was observed in measured structures. It can be explained by small size of magnetic particles or clusters, which were smaller than 40 nm and can hardly be observed on rough surfaces by MFM. Otherwise, no magnetic structures were found due to small concentration of embedded iron particles.

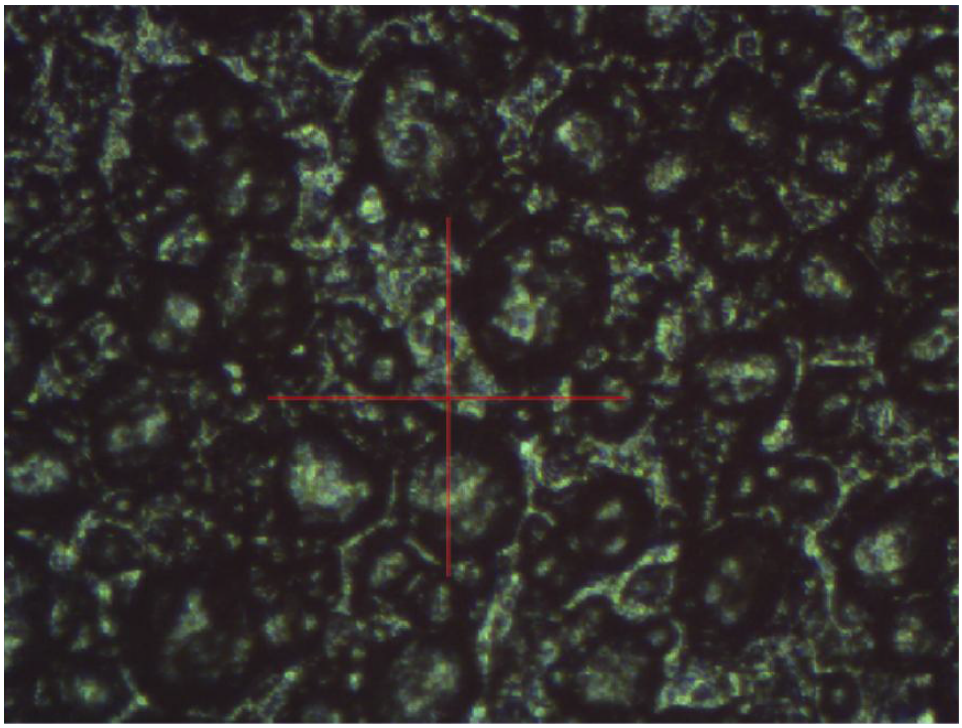

Figure 14. Aiming to surface of polystyrene/MWCNT composite film by optical microscope of AFM setup.

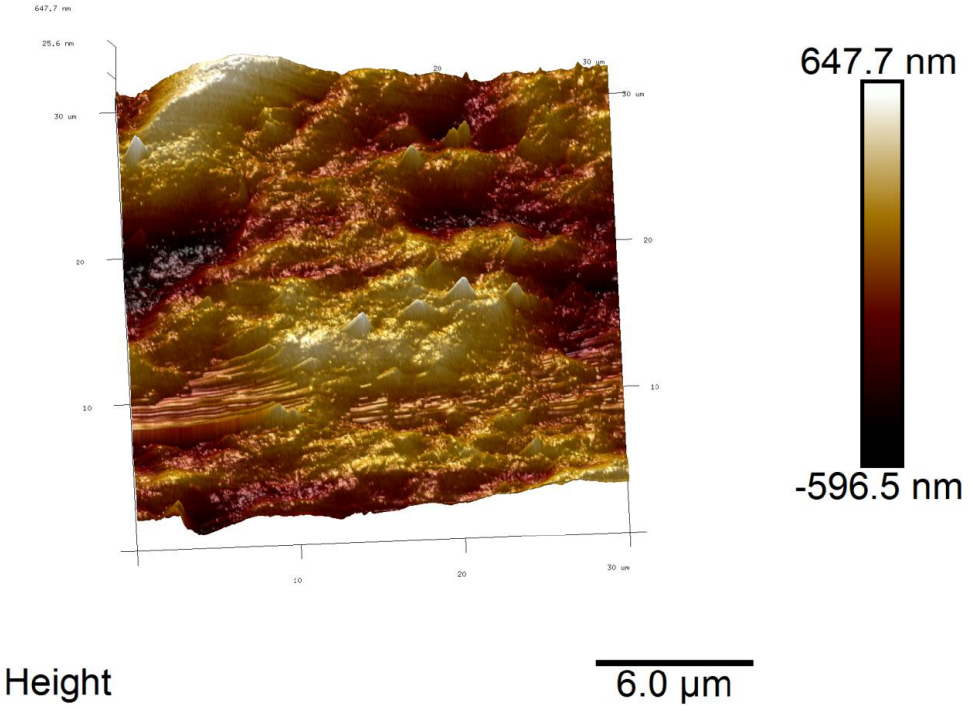

Figure 15. Surface morphology of polystyrene/MWCNT composite as seen by AFM.

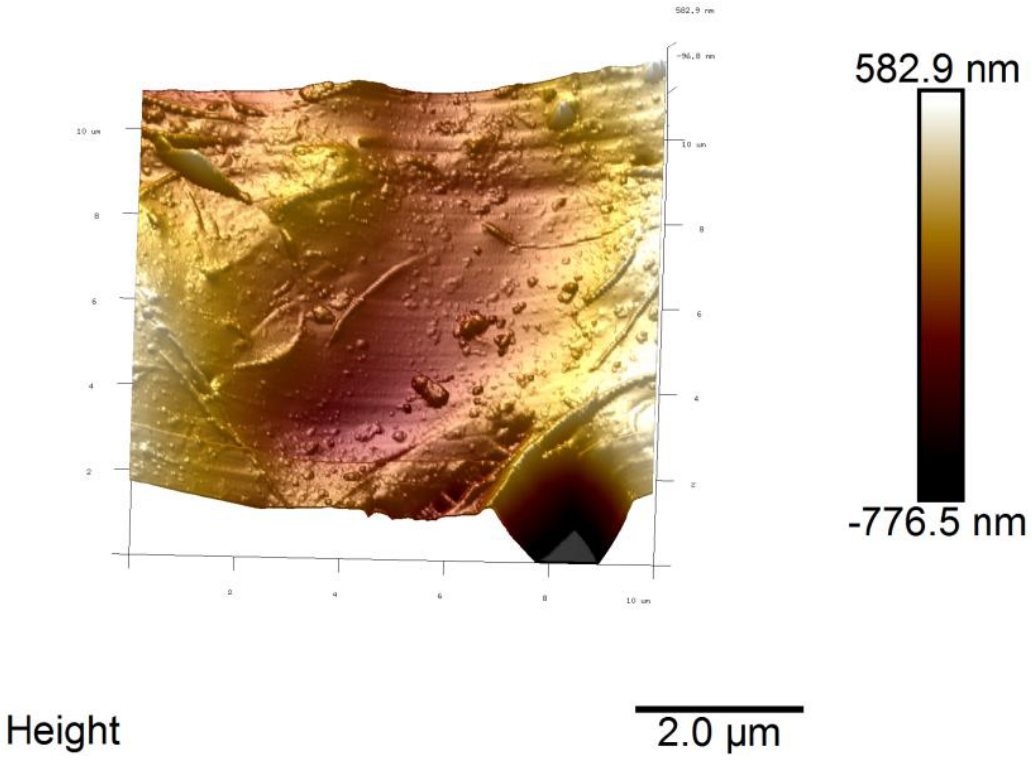

Figure 16. Surface morphology of polystyrene/MWCNT composite with higher resolution.

The AFM image shows heterogeneous surface topography. Magnetic Force Microscopy (MFM) detected no magnetic structure. The pictures of the optical microscope on the sample can be seen broad (~ 30 microns) depression. The size of the Red Cross in Figure 14 is 150 microns (one of the pictures). Magnetic cards of 10 and 16 microns showed no magnetic structure of the samples. The signal phase in the second pass ASM is responsible for the magnetic data, especially repeats topography. A distance in this passage was 70 nm and the sample that minimizes the contribution of the topography of the surface, preserving the magnetic data.

6 Measurement device

Quantum Design's Magnetic Property Measurement System (MPMS) is a very incorporated instrument framework, intended to be an essential examination device in the convoluted investigation of magnetism in matter. Intrinsic spin and orbital angular momentum is the magnetic signature of a material . On account of a material that would typically be perceived as emphatically magnetic, i.e., the ferromagnets, utilized as a part of electric motors or the material utilized on magnetic recording tape, deciding a "magnetization curve" over a scope of connected magnetic fields will help build its business esteem for a specific application. The same investigation for other materials, those that might be characterized by most people as “non-magnetic” may uncover data about electronic structure, interactions between neighboring molecules or the character of a transition between two phases of the material.

The basic components of this measurement system comprise the following:

1) Temperature Control System. Precision control of the sample temperature in the range 2 K (-271 °C) to 400 K (127 °C). This requires controlling heat flow into the sample space and the active control of gas to provide cooling power.

2) Magnet Control System. Current from a power supply is set to provide magnetic fields from zero to positive and negative one tesla. The magnet can be operated in either persistent or non-persistent modes, and several charging options can be selected by the user.

3) Superconducting SQUID Amplifier System. The rf SQUID detector is the heart of the magnetic moment detection system. It provides reset circuitry, auto-ranging capability, a highly balanced second-derivative sample coil array and EMI protection.

4) Sample Handling System. The ability to step and rotate the sample smoothly through the detection coils without transmitting undue mechanical vibration to the SQUID is of primary importance. This facility allows varied scan lengths and options as to how data are acquired for a given measurement.

5) Computer Operating System. All operating features of the MPMS are under automated, computer control. The user interface at the PC console provides the option of working under standard sequence controls, or diagnostic controls which will invoke individual functions.

The Model MPMS test magnetometer is presently utilized as a part of examination research centers around the world, and is indicated for experimental and materials characterization assignments that require the most noteworthy recognition sensitivities over a wide temperature range, and in connected magnetic fields to one tesla. This device was constructed to recognize the magnetic moment of a specimen of material, from which the magnetization and magnetic susceptibility can be resolved.

For the MPMS, superconductivity is the discriminating empowering innovation that accommodates both the creation of extensive, exceptionally stable magnetic fields, and the capacity to gauge changes in those fields which are 14 times of magnitude smaller.

The principal and most clear advantage of a superconducting material is that a lot of electrical current can be gone through it without dispersing vitality as warmth. Josephson junction is another very important part of small-scale superconducting technology. Josephson junctions have been since quite a while ago studied in superconducting computing circuits and can execute as computerized exchanging components equipped for changing states in a couple of picoseconds. Due to such structures direct observation of quantum electrodynamic phenomena is allowed. If put together in one array of thousands of identical junctions, it will be possible to fabricate a primary voltage calibration standard, which is based upon the ratio 2 e/h.

SQUID (Superconducting QUantum Interference Device) is a well-spreaded example of Josephson junction usage. A SQUID gadget comprises of a shut superconducting circle including a couple Josephson junction inside the loop's current path. The SQUID is capable of resolving changes in external magnetic fields that approach 10^{-15} tesla due to the quantized state of the superconducting ring, and the uncommon non-linear action of the Josephson junction, yet can be made to operate in fields as large as 1 tesla. The Model MPMS gets its uncommon sensitivity to the magnetic moment of materials due to an rf SQUID device.

6.1 System components

1. Sample Rod
2. Sample Rotator
3. Sample Transport
4. Probe Assembly
5. Helium Level Sensor
6. Superconducting solenoid
7. Flow Impedance
8. SQUID Capsule with Magnetic Shield
9. Superconducting Pick-up Coil
10. Dewar Isolation Cabinet
11. Dewar
12. HP Thinkjet Printer
13. Magnet Power Supply
14. Model 1802 Temperature Controller
15. Console Cabinet
16. Power Distribution Unit
17. Model 1822 MPMS Controller
18. Gas/Magnet Control Unit
19. HP Vectra Computer
20. Monitor

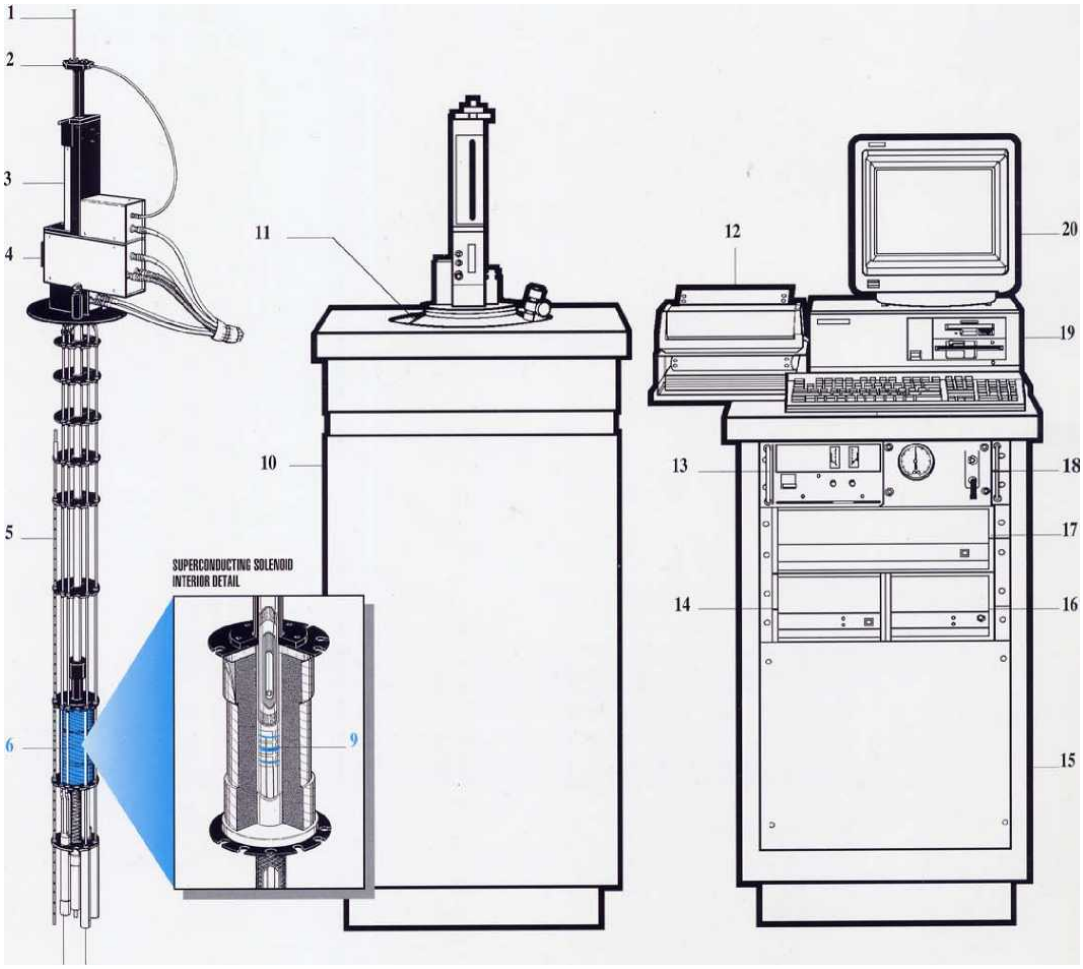

Figure 17. The appearance of Quantum Design's Magnetic Property Measurement System (MPMS).

The measurement device consists of several superconducting components:

1. a superconducting magnet to generate strong magnetic fields
2. a superconducting detection coil which couples inductively
3. a Superconducting Quantum Interference Device (SQUID) connected to the detection coil
4. a superconducting magnetic shield surrounding the SQUID

The location of the various components are shown in Figure 17 above.

6.2 SQUID

A SQUID is the most delicate gadget accessible for measuring magnetic fields. In spite of the fact that the SQUID in the MPMS is the wellspring of the instrument's remarkable sensitivity, it doesn't identify straightforwardly the magnetic field from the sample. Rather, the sample travels through an arrangement of superconducting identification coils which are associated with the SQUID with superconducting wires, permitting the current from the detection coils to inductively couple to the SQUID sensor. If properly configured, the output voltage of the SQUID is directly proportional to the current traveling in the SQUID input coils. An estimation is performed in the MPMS by moving a sample through the superconducting detection coils, which are situated outside the sample chamber and at the middle of the magnet. As the sample travels through the loops, the magnetic moment of the sample induced an electric current in the detection coils. Since the detection loops, the connecting wires, and the SQUID data loop structure a shut superconducting circle, any change of magnetic flux in the identification curls delivers a change in the persistent current in the detection circuit, which is relative to the change in magnetic flux.

6.3 The measurement procedure

The sample is mounted in a sample holder that is attached to the end of a tough sample rod. The sample rod enters the sample space through a special type of double seal (called a lip seal) designed to allow the rod to be actuated by a drive mechanism located outside of the chamber. The component containing the lip seals is damped onto the top of the airlock with standard O-ring seals, forming the top of the sample space.

The top of the sample transport rod is attached to a stepper-motor-controlled platform which is used to drive the sample through the detection coil in a series of discrete steps. It is possible to use discrete steps because the detection coil, SQUID input coil, and connecting wires form a complete superconducting loop. A change in the sample’s position causes a change in the flux within the detection coil, thereby changing the current in the superconducting circuit. Since the

loop is entirely superconducting, the current does not decay as it would in a normal conductor. During the measurement the sample is stopped at a number of positions over the specified scan length, and at each stop, several readings of the SQUID voltage are collected and averaged. The complete scans can be repeated a number of times and the signals are averaged to improve the signal-to-noise ratio.

The currents induced in the detection coil are ideally those associated with the movement of a point-source magnetic dipole through a second-order gradiometer detection coil. The spatial (position) dependence of the ideal signal is shown in Figure 18. To observe this signal requires that the sample is much smaller than the detection coil and the sample must be uniformly magnetized. Uniform magnetization, however, is often not encountered with high critical-current density (J_c) superconductors. This and other kinds of nonuniform magnetization can be a problem. In addition to this, the size and shape of a sample can also require special consideration. If a sample is very long, extending well beyond the coil during a scan, its motion in the gradiometer will not be observable, since there would be no net change of the flux in the detection coil. This is the reason that a long uniform tube can be used as a sample holder. In contrast to this, when the sample is short, the current in the detection coil changes with sample position. This is because different amounts of flux exist in each loop of the detection coil. So, it is important to realize that there is a limit on the length of a sample for which accurate measurements can be made. Some accommodation for length is made in particular computer fitting routines used to extract the value of the moment from the SQUID output. However, the safest procedure is to calibrate the MPMS with standards having a size and shape similar to the samples to be measured [48].

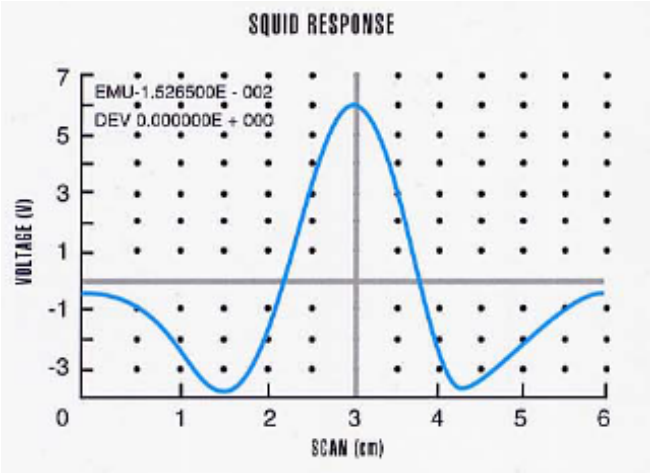

Figure 18. The output of the SQUID as a magnetic dipole is moved through the second-order gradiometer pickup coil. The vertical scale corresponds to an output voltage and the horizontal scale is sample position [48].

6.4 Atomic force microscopy

Atomic force microscopy (AFM) or scanning force microscopy (SFM) is a very high-resolution type of scanning probe microscopy (SPM), with demonstrated resolution on the order of fractions of a nanometer, more than 1000 times better than the optical diffraction limit.

The AFM contains a special sharp tip (probe) which is called cantilever that is used to scan the specimen surface. The cantilever is typically made of silicon or silicon nitride. The cantilever tip size is in the order of nanometers. When the tip is placed into proximity of a sample surface, interaction between the tip and the sample leads to a deflection of the cantilever according to Hooke's law [45]. Depending on the situation, forces that are measured in AFM include mechanical van der Waals forces, contact force, chemical bonding, capillary forces, electrostatic forces, magnetic forces, salvation forces, Casimir forces, etc. Along with force, additional values may at the same time be measured through the use of specialized types of probes. The deflection is measured by a laser spot reflected from the top surface of the cantilever. The reflected laser ray falls into an array of photodiodes. Also there are methods that are used include optical interferometry, capacitive sensing or piezoresistive AFM cantilevers. These cantilevers are fabricated with piezoresistive elements that act as a strain gauge. Using a Wheatstone bridge, strain in the AFM cantilever due to deflection can be measured, but this method is not as sensitive as laser deflection or interferometry.

When tip is scanned at a constant height, there is a risk of damaging surface by collision with the tip. That is why, in most cases there is a special feedback mechanismwhich helps to adjust the distance between tip and sample to maintain a constant force between the tip and the sample. As usual the tip or sample is mounted on a 'tripod' of three piezo crystals, with each responsible for scanning in the *x*,*y* and *z* directions [46]. In 1986, the same year as the AFM was invented, a new piezoelectric scanner, the tube scanner, was developed for use in STM [49]. Later tube scanners were incorporated into AFMs. The tube scanner can move the sample in the *x*, *y*, and *z* directions using a single tube piezo with a single interior contact and four external contacts. An advantage of the tube scanner is better vibrational isolation. As a result the higher resonant frequency of the single-crystal construction in combination with a low resonant frequency isolation stage. A drawback is that the *x*-*y* movement can cause unwanted *z* motion resulting in misrepresentation.

There are several ways of the AFM operation which depend on the application. Generally, modes of imaging are divided into static (also called contact) modes and a variety of dynamic (non-contact or "tapping") modes where the cantilever is vibrated or oscillated at a given frequency [50].

7 Sample preparation

Because of some restriction made by measurement device sample holder and because of measurement technique, samples should be prepared in specific way. Also some special geometric parameters were used because magnetic response is studied. One thin film gives small magnetic response, that is why we used several thin films stacked on each other. The films should be stacked in special direction to each other to preserve any anisotropy contained within original material.

As it was mentioned above studied samples initially were thin films. Hence they did not correspond to required parameters. Also the whole sample is not required. As it can be clearly seen in Figure 19 below the sample has maximum anisotropy not along the entire length.

Because the sample was fastened at the ends and stretched, so maximum stretched region is in the center of the sample. Hence, the expected anisotropy should be maximum in the center part of the sample.

Figure 19. Initial sample.

Only middle part which is marked by high lighter consist maximum anisotropy. That is why in order to prepare proper sample the middle part should be cut out from the sample. Although even clipped middle part will not be fitted into sample holder and it still does not have height and as a result it is not volumetric. Thus middle part should be cut into several pieces. All the pieces should be stuck together one another. The direction of this pieces during sticking is also important to preserve any anisotropy contained within original material.

Nonmagnetic tape, nonmagnetic scissors and nonmagnetic tweezers are required in order to make all the operation mentioned above. All the equipment are represented in Figure 20 below.

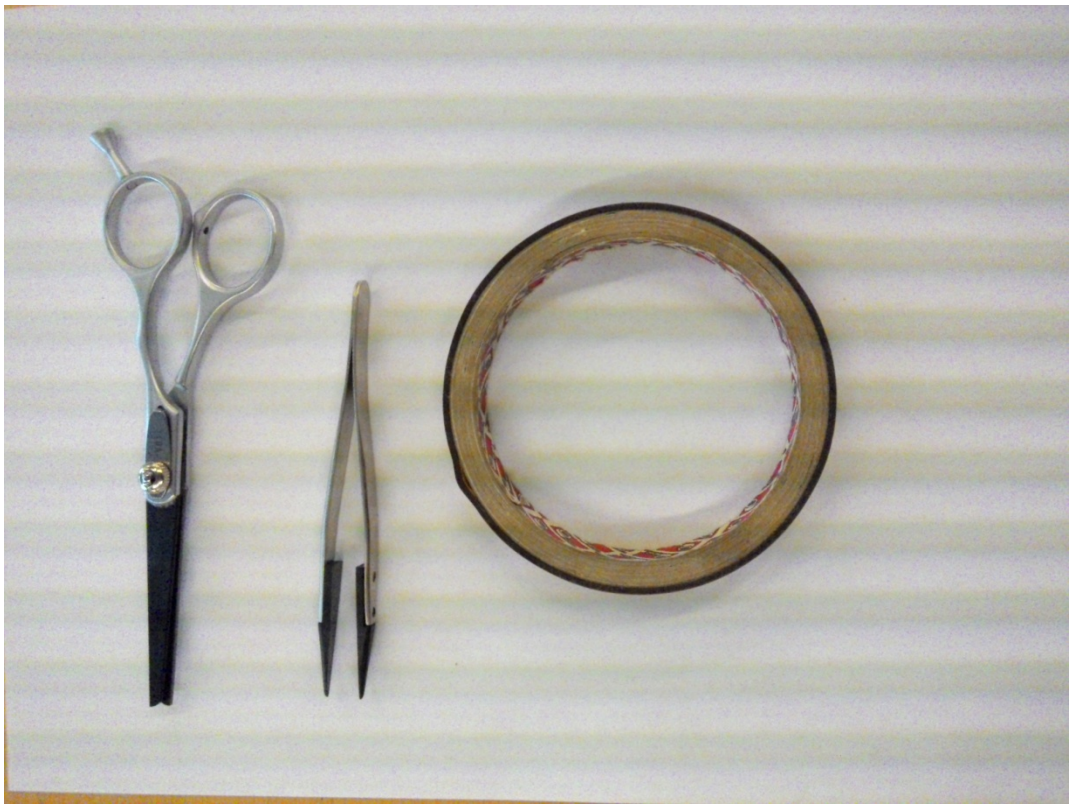

Figure 20. Used tools. Scissors, tweezers and tape.

The nonmagnetic tape is made from Kapton ® HN film with silicone adhesive. It could be used in wide range of temperatures from -269°C to 260°C. [51] The only difference of nonmagnetic scissors and nonmagnetic tweezers between ordinary one is ceramic blades for scissors and ceramic tips.

Firstly the thin film was split into six small pieces. Each piece was marked by highlighter from one side. It was made in order not to change the direction of stretching the sample. Secondly all the pieces were weighed. Thirdly all the pieces were stuck together into one big. The final result is shown in Figure 21 below.

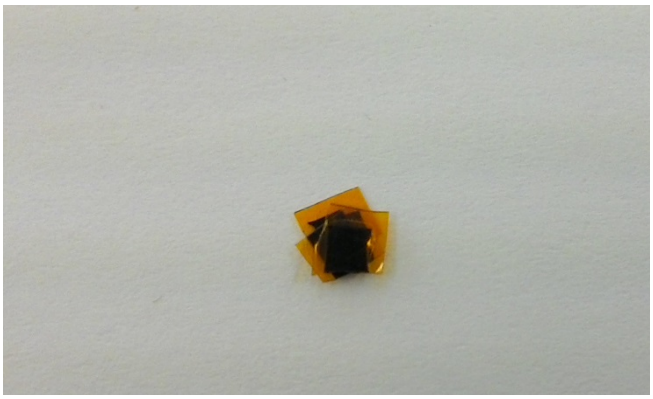

Figure 21. Prepared sample.

Finally finished sample was placed into plastic tube as shown on Figure 22 below.

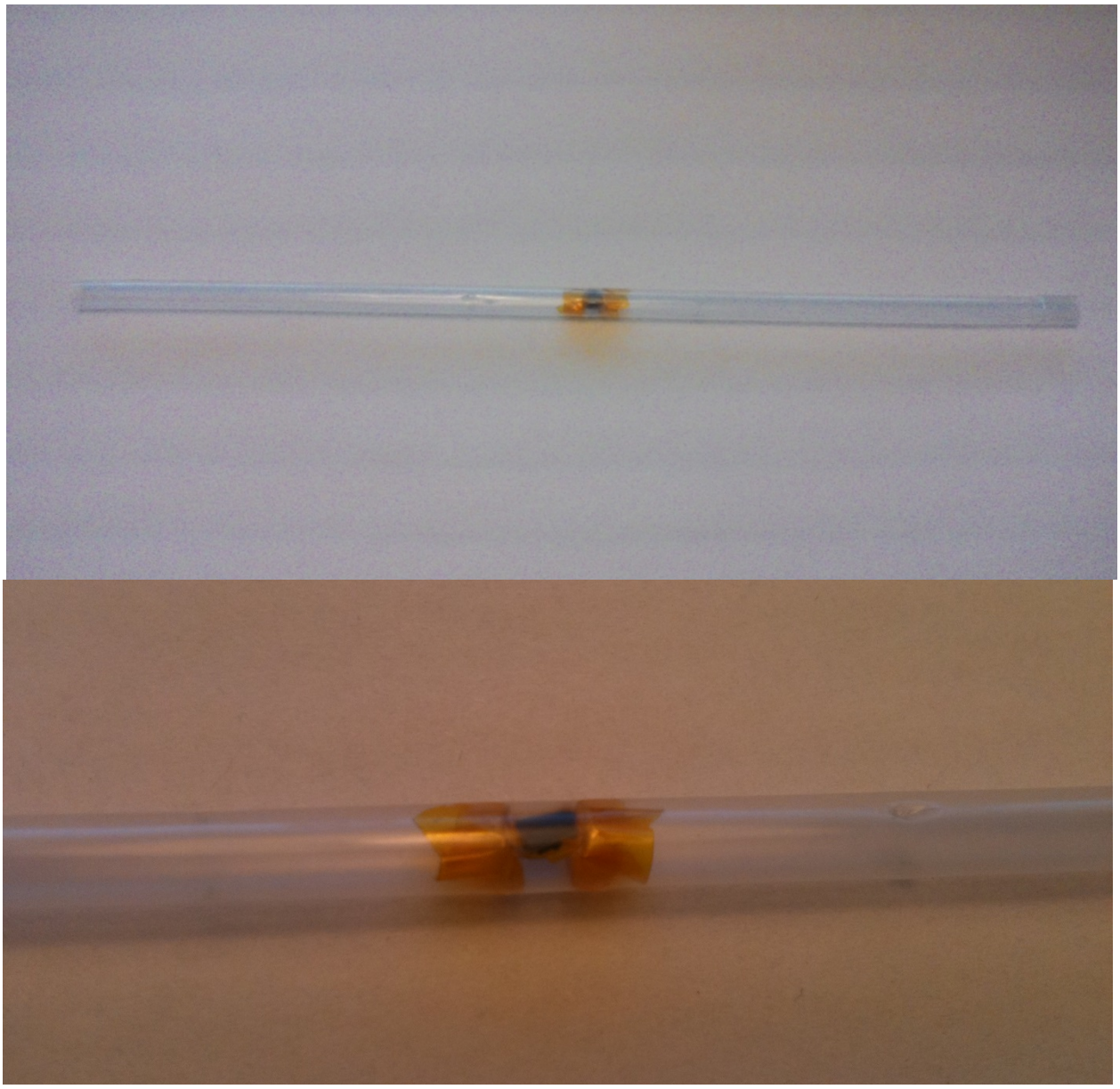

Figure 22. Sample in the tube.

Now this sample is ready to be investegated in the MPMS. All the operations which is mentioned above were made with all samples.

8 Experiment process

In the beginning of the experiment obtained plastic tube with the sample is attached to long sample rod. Then the structure is installed into the cryostat. The temperature inside the cryostat is lowered to 3 K. After achieving thermal equilibrium the measurement starts.

In order to measure magnetic moment versus field, the temperature is kept constant and magnitude of external field is changing. The field changing step is 500 Oe in the range from 0 Oe up to 5000 Oe and 1000 Oe from 5000 Oe till 10000 Oe. The same manipulation was made with opposite magnetic field direction. Then the temperature is changed to another value and the sequence is repeated with parameters mentioned above.

The temperature dependence of magnetic moment was made in two regimes:

1. zero field cooling (zfc)
2. field cooling (fc)

The sample is cooled to 3 K in zero magnetic field. Then magnetic field is turned on, for instance, $H = 1$ kOe. Next the sample is warmed up to 400 K and data is collected during this process. This is so called zero field cooling. Then the applied field stays the same and the cooling begins until lowest temperature equals 3 K. This manipulation is called field cooling. Eventually, the field turns off and the experiment is done.

9 Obtaned results

As it was mentioned above the magnetization behavior versus magnetic field with different temperature were made and also magnetization behavior versus temperature with different magnetic field were made. Firstly, magnetization versus magnetic field will be considered. Secondly, magnetization versus temperature will be considered. Overall, the conclusion will be made.

9.1 The dependence of magnetization on magnetic field

Figures 23, 24, 25 below show the dependence of magnetization on magnetic field for 1 wt% sample but with different temperature. To get this results the sample were placed into the MPMS. The applied magnetic field to the sample was changing while the temperature was the same 3 K, 100 K and 300 K.

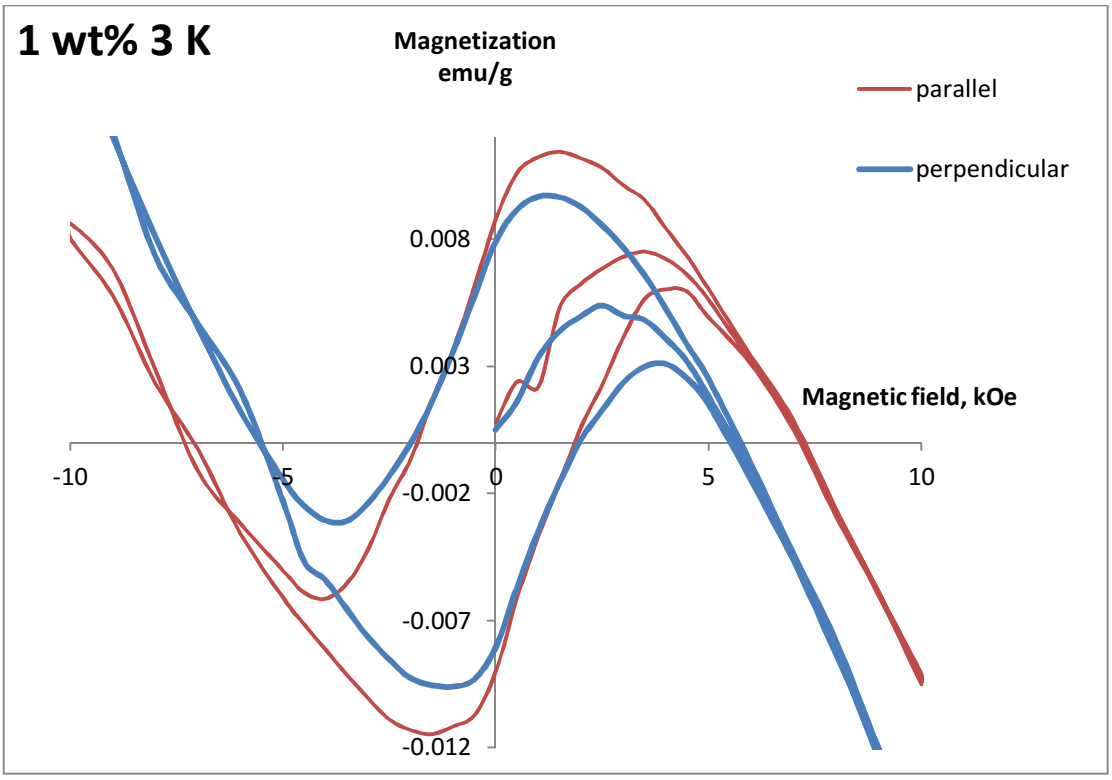

Figure 23. The dependence of magnetization on the magnetic field for 1 wt% sample at 3 K temperature. In different direction of magnetic field according to sample axis.

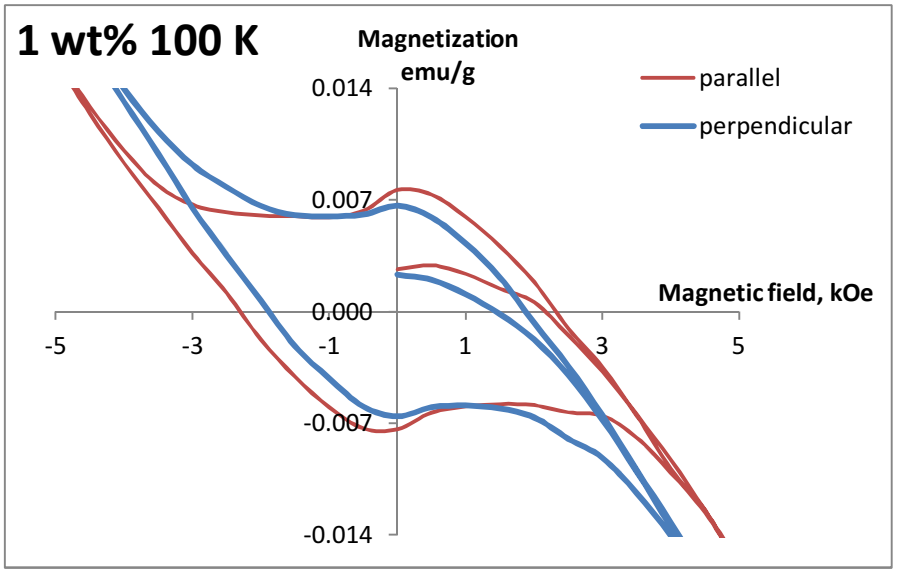

Figure 24. The dependence of magnetization on the magnetic field for 1 wt% sample at 100 K. In different direction of magnetic field according to sample axis.

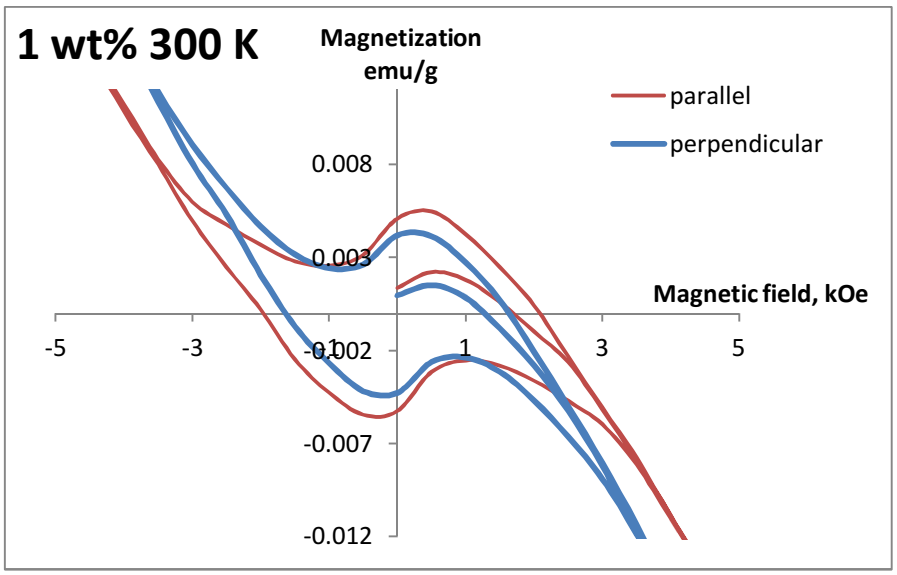

Figure 25. The dependence of magnetization on the magnetic field for 1 wt% sample at 3 K. In different direction of magnetic field according to sample axis.

The Figures 23, 24, 25 compare behavior of magnetization of the sample with different direction of the magnetic field. As shown in pictures above all the dependences show hysteresis. As it could be clearly seen, the curves related to magnetization of the sample in different direction of the magnetic field do not match each other. This shows that there is some magnetic anisotropy present in the material. The parameters of the hysteresis loops will be calculated below.

In order to get the parameters of the ferromagnetic hysteresis loops we should subtract diamagnetic component prevailing at high fields. The diamagnetic component have to be deducted from original loops. The equation for hysteresis without diamagnetic component:

$$M_c = M(H) - k * H \quad (11)$$

where k is the slope coefficient of the diamagnetic component.

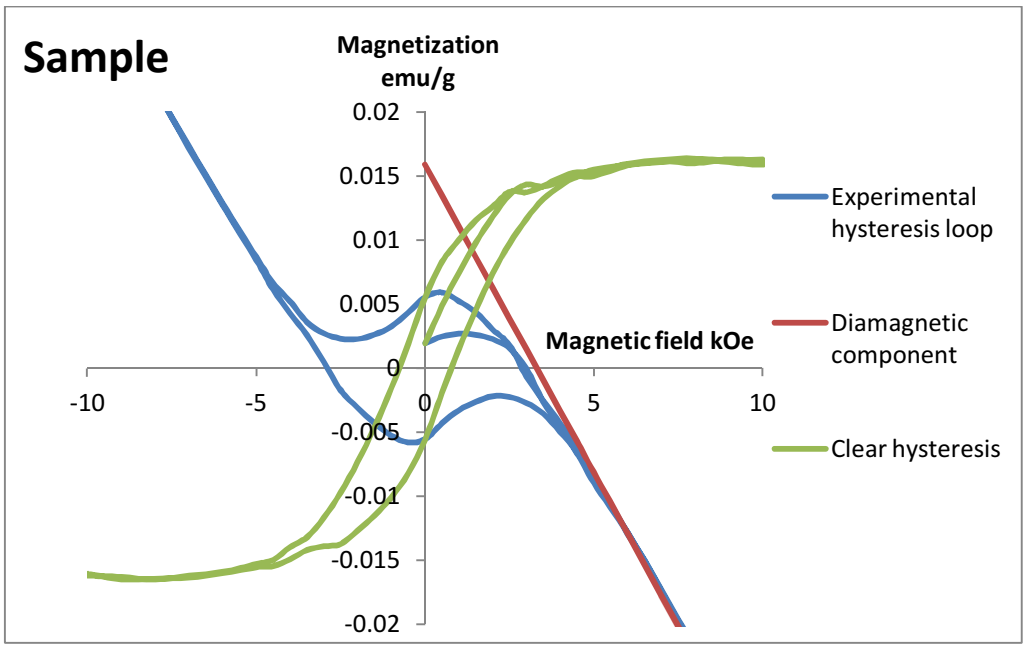

Figure 26. The example of subtraction of diamagnetic component for sample 1 wt% stretched at 100 K.

Figure 26 represents the process of deduction of the diamagnetic component from experimental hysteresis loop.

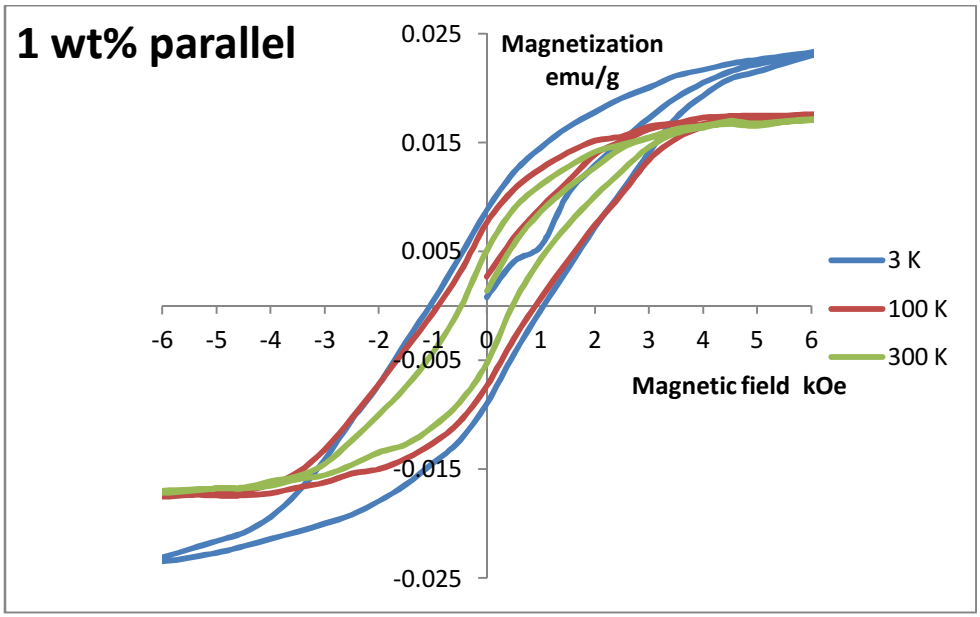

Figure 27. Ferromagnetic hysteresis of 1 wt% sample with field direction parallel to the axis of stretching at temperature 3 K, 100 K and 300 K.

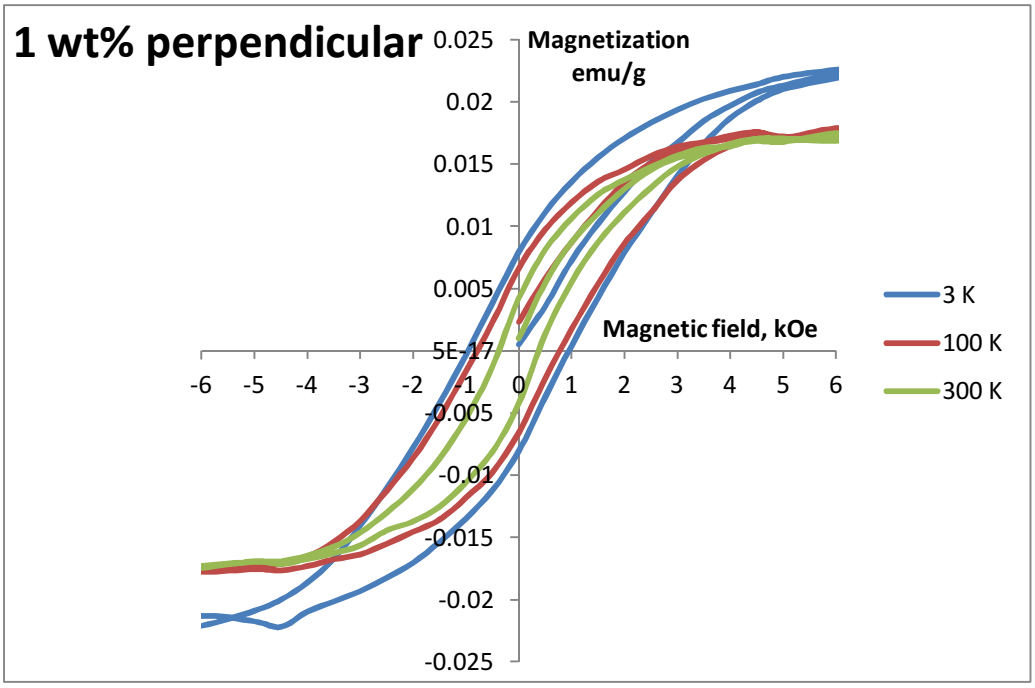

Figure 28. Ferromagnetic hysteresis loops of 1 wt% sample for perpendicular field direction and at temperature 3 K, 100 K, 300 K.

Table №4 represents the parameters of hysteresis loops shown on Figure 28 above.

Table 4. Coercivity (Hc), remanent magnetization (Mr) and saturation magnetization (Ms).

	Hc_paral (Hc_perp), (Oe)	Mr_paral (Mr_perp), emu/g	Ms_paral (Ms_perp), emu/g
3 K	500 (1000)	0.0123 (0,0079)	0.0222 (0,0213)
100 K	480 (900)	0.0107 (0,0067)	0.0171 (0,0179)
300 K	450 (400)	0.0089 (0,0081)	0.0165 (0,0168)

The dependence of coercivity, remanent magnetization and saturation magnetization on temperature can be clearly seen from the Table №4. For sample in parallel field direction the coercivity smaller than for sample in perpendicular field direction. In both experiments the coercivity goes down with temperature increase. The remanent magnetization in the case of parallel direction of the field is also bigger than in case of perpendicular dependence and also decreases with temperature rise. As for saturation magnetization it also reduces with temperature increase.

From data above another dependence could be obtained. The information for magnetization versus temperature behavior is represented in Table 5.

Table 5. Magnetization and temperature of 1 wt% sample.

T, K	1 wt% parallel	1 wt% perpendicular
3	0.01144	0.00966
100	0.0041	0.00216
300	0.00248	0.00069

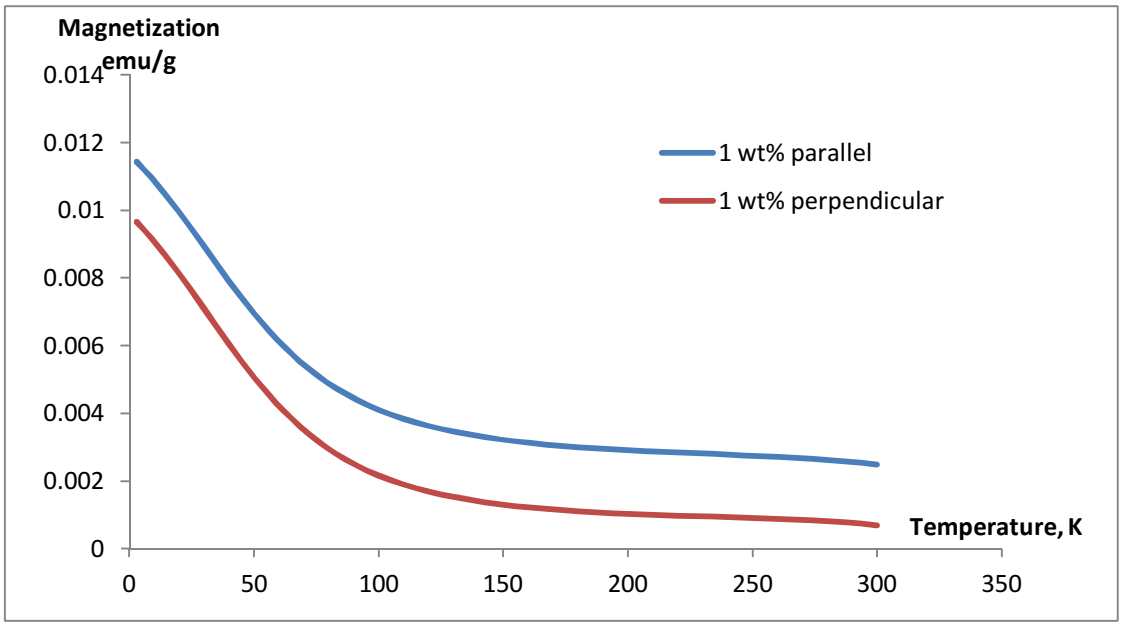

Figure 29. The magnetization versus temperature dependence for sample in parallel and perpendicular magnetic field.

As it could be clearly seen the magnetization of the sample in both types of field direction decreases with temperature increase. The temperature region below 100 K is characterized by relatively large parametric signal from the samples increasing as the temperature is lowered. This can be understood as decrease of thermal influence on magnetic interaction between ion nanoparticles. Below 100 K the exchange interaction become larger in comparison to the thermal energy. The diamagnetic anisotropy of the magnetic system is clearly visible in Figure 29. It is equal to the difference between the two curves.

The low temperature increase in magnetization can be attributed to the ferromagnetic part of the material. As the temperature becomes higher the diamagnetic part influence on the magnetization more. This leads the M(T) curves closer to 0 value.

The Figures 30, 31 below show the dependence of magnetization on magnetic field for 2,5 wt% sample at different temperatures. To get this results the sample were placed into the MPMS. The magnetic field which were applied to the sample was changing while the temperature was the same 3 K, 100 K.

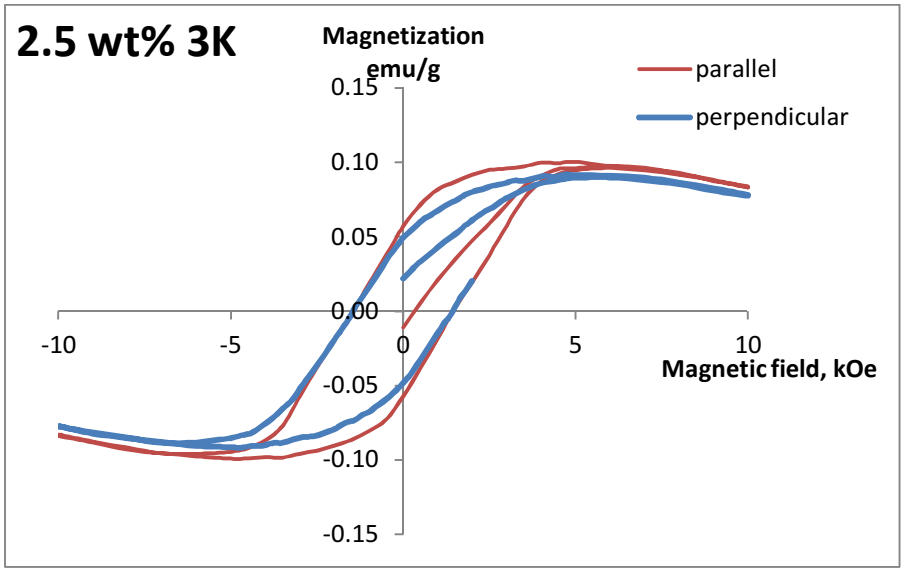

Figure 30. The dependence of magnetization on the magnetic field for 2,5 wt% sample at 3 K.

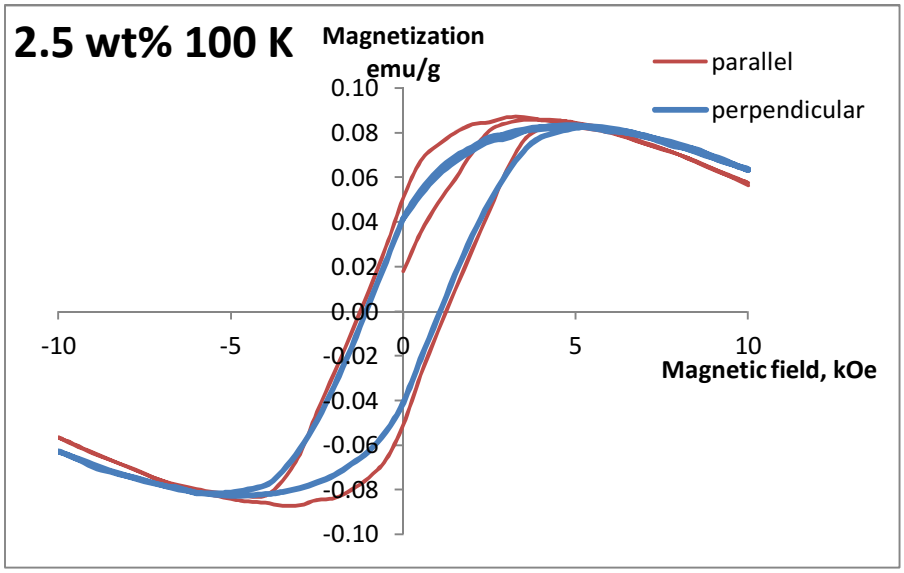

Figure 31. The dependence of magnetization on the magnetic field for 1 wt% sample at 100 K.

The Figures 30, 31 compare behavior of magnetization of the sample with different direction of the magnetic field. As shown in pictures above all the dependence represent hysteresis. As it can be clearly seen the curves related to magnetization of the sample in different direction of the magnetic field do not match each other. The parameters of the hysteresis loops will be calculated below. The method of parameters calculation is described above.

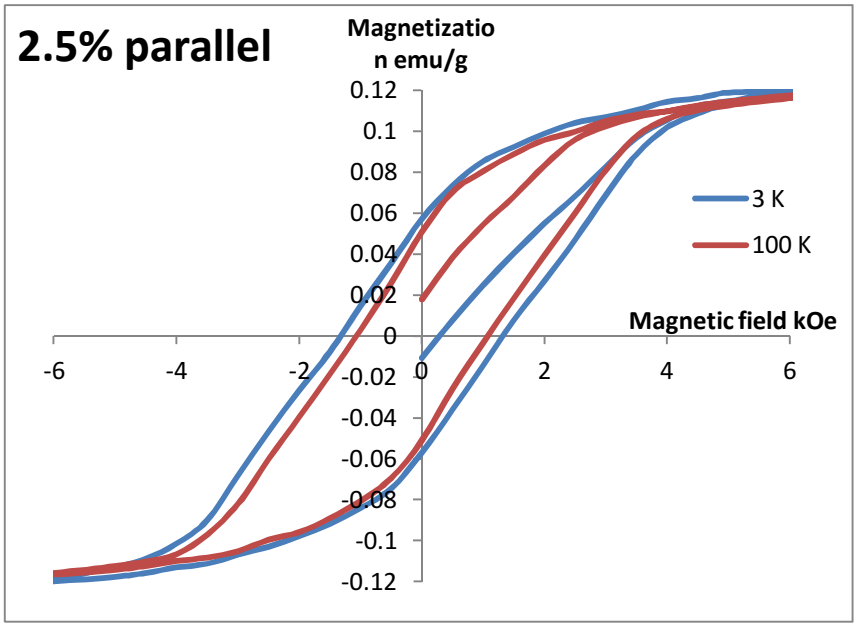

Figure 32. Ferromagnetic hysteresis loops of 2.5 wt% sample with parallel field direction at temperature 3 K and 100 K.

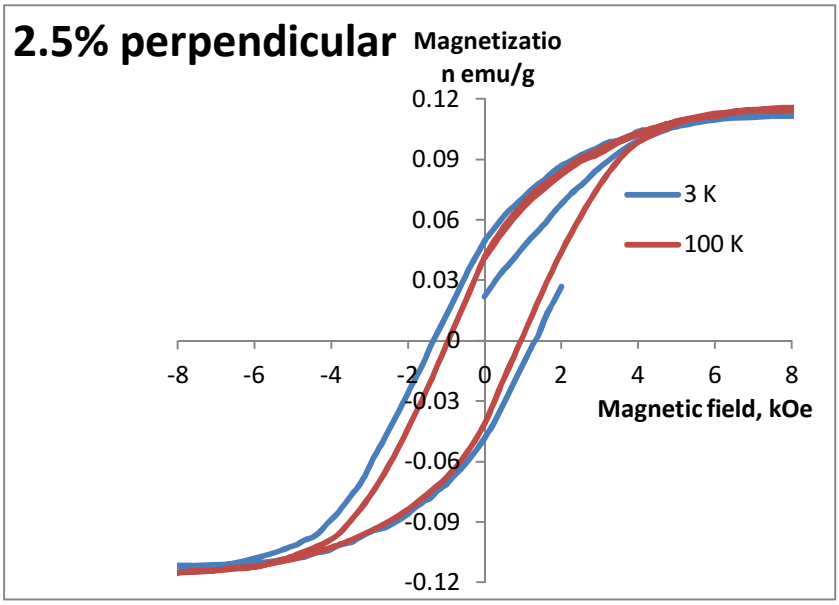

Figure 33. Ferromagnetic hysteresis loops of 2,5 wt% sample with parallel field direction at 3 K and 100 K.

Table №6. Coercivity (Hc), remanent magnetization (Mr) and saturation magnetization (Ms).

	Hc_paral (Hc_perp), (Oe)	Mr_paral (Mr_perp), emu/g	Ms_paral (Ms_perp), emu/g
3 K	1100 (1200)	0.05706 (0.04149)	0.1160 (0.1145)
100 K	1000 (1050)	0.05078 (0.04138)	0.1144 (0.1115)

The dependence of coercivity, remanent magnetization and saturation magnetization on temperature could be clearly seen from the Table 6. For sample in parallel field direction the coercivity smaller than for sample in perpendicular field direction. In both experiments the coercivity goes down with temperature increase. The remanent magnetization in the case of parallel direction of the field is also bigger than in case of perpendicular dependence and it also decreases with temperature rise. As for saturation magnetization it also reduces with temperature increase. The different result depending on the magnetic field direction relative to the sample can be explained by shape anisotropy of the iron particle assembling.

In order to describe the influence of the nanotubes on the properties of the samples the multiwall carbon nanotubes (MWCNT) array was studied also. MWCNTs were initially grown on silicon (Si) substrate. SEM analysis shown that the nanotubes are perpendicular to the Si substrate. [51] The Figures 36 and 37 below show the dependence of magnetization on magnetic field for MWCNT sample with different temperature. To get this results the sample were placed into the MPMS. The magnetic field which was applied to the sample was changing while the temperature was the same 3 K, 100 K.

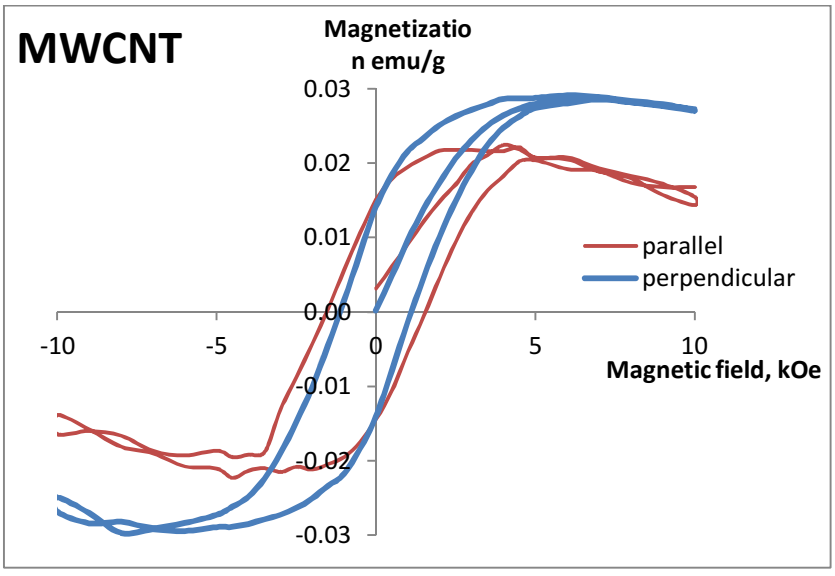

Figure 34. The dependence of magnetization on the magnetic field for MWCNT sample at 3 K.

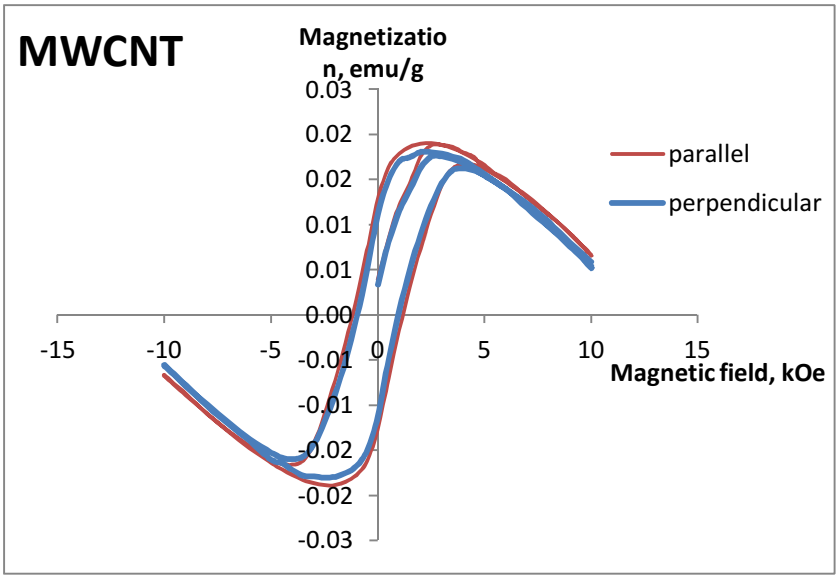

Figure 35. The dependence of magnetization on the magnetic field for MWCNT sample at 100K.

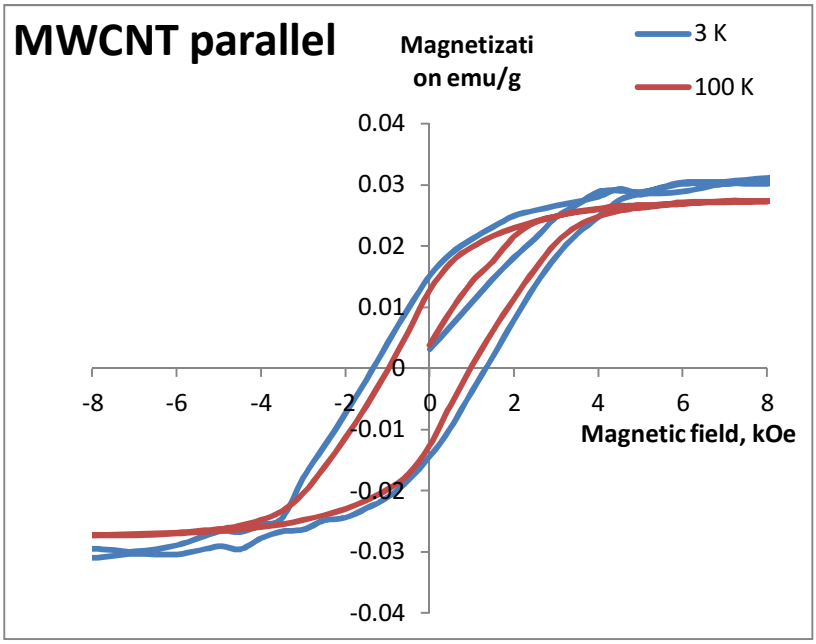

Figure 36. The dependence of magnetization on the magnetic field for MWCNT at 3 K and 100 K for parallel configuration.

Perpendicular regime of measurements displays considerable diamagnetic contribution to the M(H) for aligned MWCNT on Si substrate. This observation shows that the alignment of MWCNTs contribute to the diamagnetic anisotropy of the composite. Hence, the total diamagnetism of the system comprise of two parts: polymer matrix and aligned nanotubes

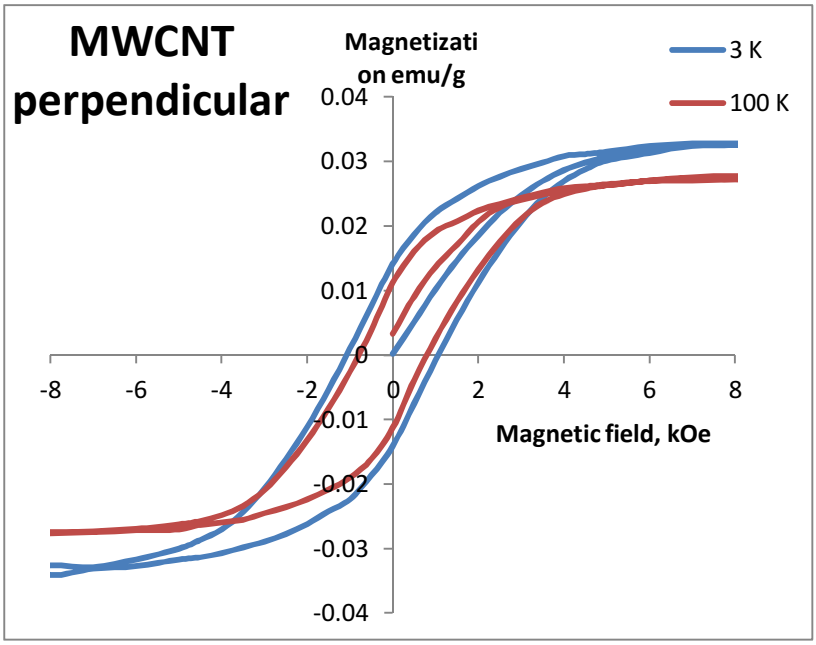

Figure 37. The dependence of magnetization on the magnetic field for MWCNT sample at 3 K and 100 K for perpendicular configuration.

Table 7. Coercivity (Hc), remanent magnetization (Mr) and saturation magnetization (Ms).

	Hc_paral (Hc_perp), (Oe)	Mr_paral (Mr_perp), emu/g	Ms_paral (Ms_perp), emu/g
3 K	1200 (1000)	0.01508 (0.01120)	0.03113 (0.03287)
100 K	1000 (900)	0.01272 (0.01414)	0.02722 (0.02772)

The dependence of coercivity, remanent magnetization and saturation magnetization on temperature can be clearly seen from the Table 7. For sample in parallel field direction the coercivity bigger than for sample in perpendicular field direction. In both experiments the coercivity goes down with temperature increase. The remanent magnetization in the case of parallel direction of the field is also bigger than in case of perpendicular dependence and also decreases with temperature rise. As for saturation magnetization it also reduces with temperature magnification. This happens due to increase of thermal energy, which ruin spontaneous magnetization of the ferromagnetic system. At higher temperatures thermal energy is big enough to flip the spins, which destroys the magnetic order.

The dependence of coercivity, remanent magnetization and saturation magnetization on temperature on amount of nanotubes in samples were also studied. In the Figure 38, below there

is visual hysteresis comparison of samples with different amount of nanotubes under the same condition.

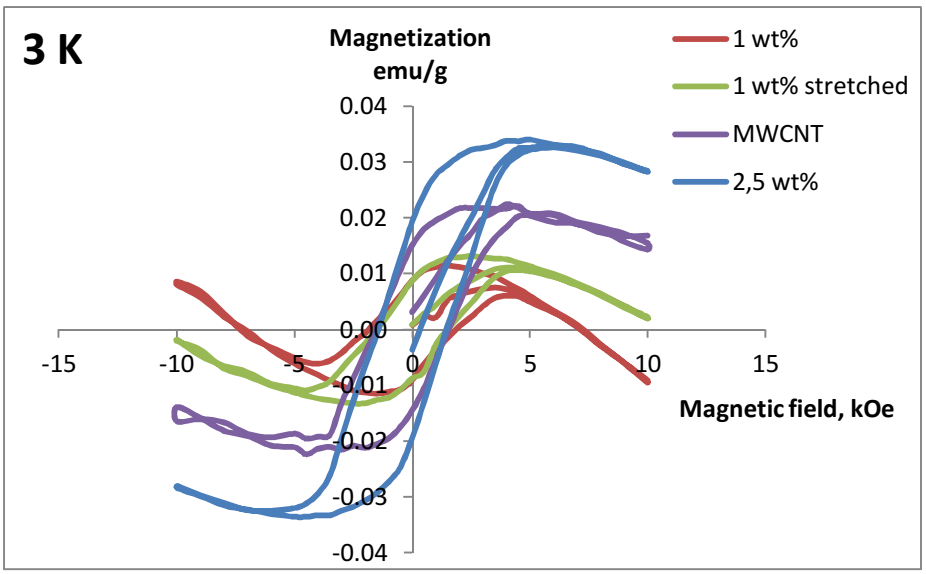

Figure 38. The dependence of magnetization on the magnetic field for 1 wt%, 1 wt% (100% stretched), 2.5 wt% and MWCNT samples at 3 K.

All the properties are collected in the Table №8 below.

Table №8. Coercivity (Hc), remanent magnetization (Mr) and saturation magnetization (Ms).

	Hc, (Oe)	Mr, emu/g	Ms, emu/g
1 wt%	500	0.0123	0.0222
1 wt% stretched	1000	0.008749	0.02332
2.5 wt%	1100	0.05706	0.1160
MWCNT	1200	0.01508	0.03113

The dependence of remanent magnetization and saturation magnetization on temperature on amount of nanotubes in the samples is not linear. Only coercivity shows linear dependence. Remanent magnetization and saturation magnetization are bigger for 2 wt% sample than for 1 wt% and 1 wt% stretched samples but smaller than for MWCNT sample.

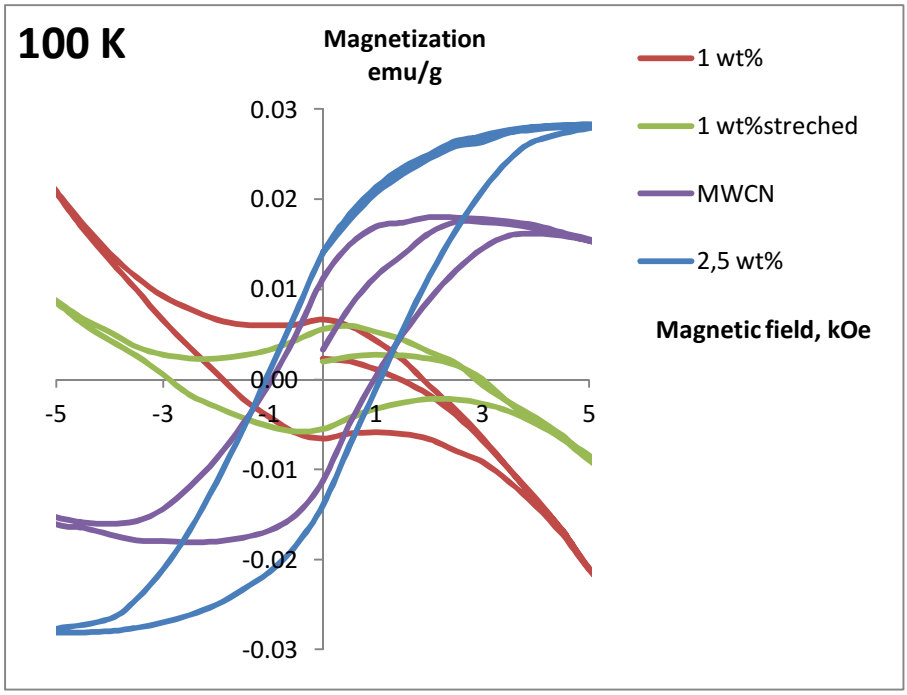

Figure 39. The dependence of magnetization on the magnetic field for 1 wt%, 1 wt% stretched, 2.5 wt% and MWCNT samples and with 100 K temperature.

Table №9. Coercivity (Hc), remanent magnetization (Mr) and saturation magnetization (Ms).

	Hc, (Oe)	Mr, emu/g	Ms, emu/g
1 wt%	900	0.0067	0.0179
1 wt% stretched	900	0.00556	0.0164
2,5 wt%	1050	0.04138	0.1115
MWCNT	900	0.01414	0.02772

The dependence of remanent magnetization and saturation magnetization on temperature on amount of nanotubes in the samples is not linear. In that case also the coercivity does not show linear dependence. Coercivity, remanent magnetization and saturation magnetization are bigger for 2 wt% sample than for 1 wt% and 1 wt% stretched samples but bigger than for MWCNT sample.

The existence of hysteresis with pronounced retentivity and coercivity gives a conclusion that the polystyrene/MWCNT composites are not supermagnetic. Hence the iron are dispersed inside the composites with density.

9.2 The dependence of magnetization on temperature

The dependence of magnetization on temperature was made for three samples: 1 wt%, 1 wt% (100% stretched) and 2.5 wt%. To obtain these results the sample were placed into the MPMS. The magnetic field was 500 Oe and temperature was changing from 3 K up to 400 K.

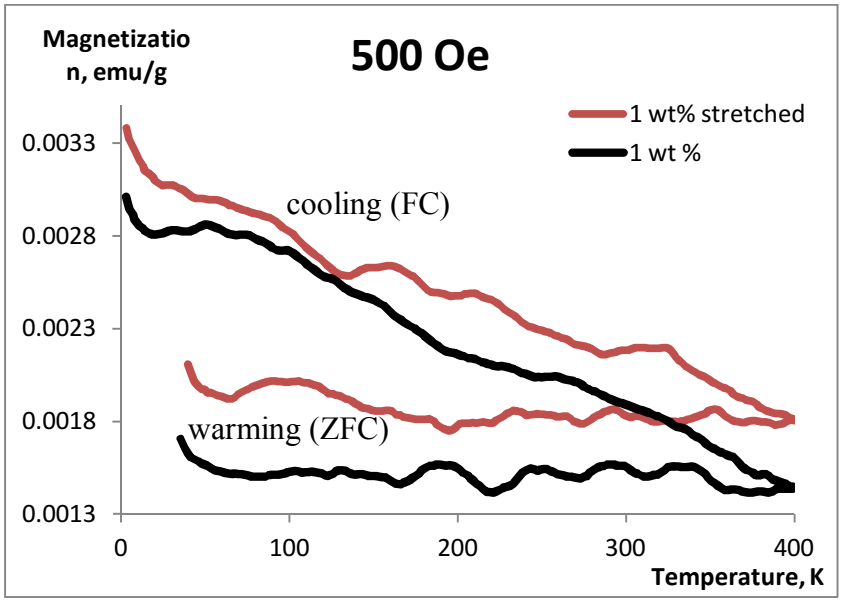

Figure 40. The magnetization versus temperature dependence for 1 wt% and 1wt% stretched samples.

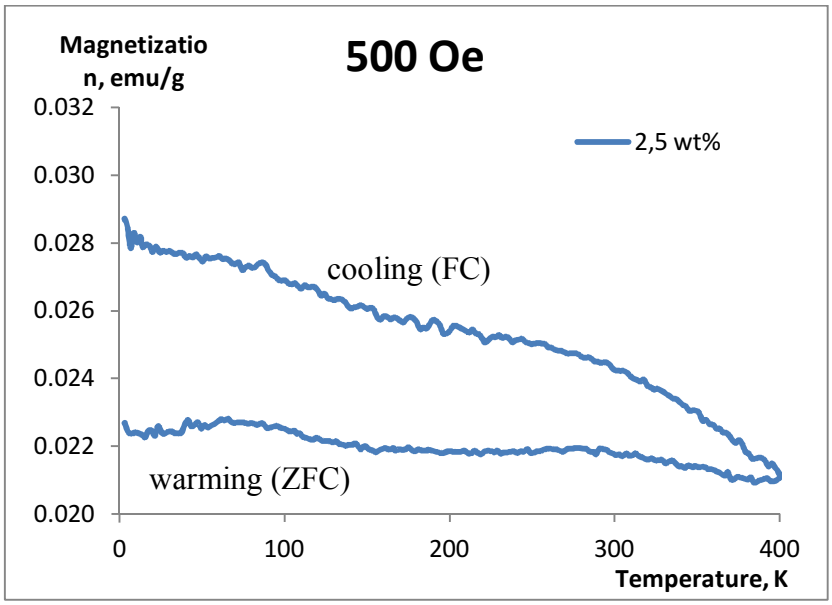

Figure 41. The magnetization versus temperature dependence for 2,5 wt% sample.

As it can be clearly seen from the Figures 42 and 43 above the magnetization decreases for both samples. Magnetization under field cooled and under zero-field cooled procedures show a division into two separate curves with decreasing temperature. The difference in FC and ZFC

magnetization suggests on existence of small magnetic domains in the material. In addition, the high transition temperature of ZFC-FC splitting implies larger magnetic domains.

Conclusion

Magnetic properties of polystyrene/multiwall carbon nanotube composite films are investigated with Quantum Design SQUID magnetometer (MPMS XL). The composites with 1 and 2.5 wt% of MWCNT loadings have been provided by Physics Chemistry of Nanomaterials laboratory, Nikolaev Institute of Inorganic Chemistry, Russia. The average ratio of length to outer diameter of the MWCNTs used in fabrication is 5000. The preparation of such composites is explained in details in literature [45].

The field dependencies of magnetization of the samples have pronounced hysteresis with clear diamagnetic contribution at high fields. The saturation magnetization, remanent, and coercivity decrease with to the decrease of MWCNTs filling amount. Subtraction of the diamagnetic contribution shows that hysteresis's properties show magnetic anisotropy. Such anisotropy is attributed to the shape anisotropy of the magnetic iron inclusions formed by the ferrocene catalyst. Also the anisotropy is observed in diamagnetic contribution with respect to the axis of polymer stretching. The sources of diamagnetism in the material are the polystyrene matrix and aligned carbon nanotubes. The investigation of the MWCNTs aligned on a silicon substrate as a reference sample shows that aligned MWCNTs have diamagnetic anisotropy.

Temperature dependences of magnetization of the films have been done in two regimes: zero-field cooled and field cooled. They show rather large difference indicating presence of magnetic inclusions which have ferromagnetic nature.

The atomic force microscopy study of the surfaces has been done with BRUKER Multimode 8 setup. The investigation revealed that the nanotubes to some extent are aligned with the axis of stretching. The magnetic force mode did not show magnetic structures in the material suggesting that the ferromagnetic nanoparticles are less than 30 nm. This is in full agreement with the fact that magnetic iron nanoparticles aggregate inside the nanotubes and tubes' inner diameter is around 10 nm.

References

1. Bychanok D, Kanygin M, Okotrub A, Shuba M, Paddubskaya A, Pliushch A, et al. 2011. Anisotropy of the electromagnetic properties of polymer composites based on multiwall carbon nanotubes in the gigahertz frequency range. *JETP Lett*, vol. 93, issue 10, pp. 607-611.
2. Kanygin MA, Sedelnikova OV, Asanov IP, Bulusheva LG, Okotrub AV, Kuzhir PP, et al. 2013. Effect of nitrogen doping on the electromagnetic properties of carbon nanotube-based composites. *J Appl Phys*, vol.113, issue 14.
3. Suslyaev VI, Kuznetsov VL, Zhuravlev VA, Mazov IN, Korovin EY, Moseenkov SI, et al. 2013. An investigation of electromagnetic response of composite polymer materials containing carbon nanostructures within the range of frequencies 10 MHz–1.1 THz. *Russ Phys J*, vol. 55, issue 8, pp. 970–976.
4. Kuzhir P, Paddubskaya A, Bychanok D, Nemilentsau A, Shuba M, Plusch A, et al. 2011. Microwave probing of nanocarbon based epoxy resin composite films: toward electromagnetic shielding. *Thin Solid Films*, vol. 519, Issue 12, pp. 4114–4118.
5. Kuzhir PP, Paddubskaya AG, Shuba MV, Maksimenko SA, Celzard A, Fierro V, et al. 2012. Electromagnetic shielding efficiency in Ka-band: carbon foam versus epoxy/carbon nanotube composites. *J Nanophoton*, vol. 6.
6. Mazov I, Kuznetsov V, Moseenkov S, Usoltseva A, Romanenko A, Anikeeva O, et al. 2009. Electromagnetic shielding properties of MWCNT/PMMA composites in Ka-band. *Phys Status Solidi B,* vol 246, issue 11-12, pp. 2662-2666.
7. Suslyaev VI, Zhuravlev VA, Dotsenko OA, Sarkisov SY, Kuznetsov VL, Moseyenkov SI, et al. 2013. Electromagnetic properties of composites based on multiwall carbon nanotubes studied by THz-TDS and cw BWO-based spectrometer at different levels of peak THz power. 23rd Int. Crimean Conf. ‘‘Microwave & Telecommunication Technology’’ (CriMiCo’2013). Sevastopol, p. 980–981.
8. Zhuravlev VA, Suslyaev VI, Dunaevskii GE, Emelyanov EV, Mazov I, Moseenkov SI, et al. 2012. Complex permittivity of polymer composites containing carbon nanostructures in frequency range 0.17–1.1 THz. 37th INT. Conf. ‘‘IRMMW-THZ’’. Wollongong.
9. Okotrub AV, Kubarev VV, Kanygin MA, Sedelnikova OV, Bulusheva LG. Transmission of terahertz radiation by anisotropic MWCNT/polystyrene. *Phys Status Solidi*, vol. 248, issue 11, pp. 2568-2571.
10. Bychanok DS, Shuba MV, Kuzhir PP, Maksimenko SA, Kubarev VV, Kanygin MA, et al. 2013. Anisotropic electromagnetic properties of polymer composites containing

oriented multiwall carbon nanotubes in respect to terahertz polarizer applications. *J Appl Phys*, vol. 114, issue 11.

11. Macutkevic J, Seliuta D, Valusis G, Adomavicius R, Krotkus A, Paddubskaya A, et al. 2012. Multi-walled carbon nanotubes/PMMA composites for THz applications. *Diamond Relat Mater*, vol. 25, pp. 13–18.
12. Paddubskaya AG, Kuzhir PP, Kuznetsov VL, Mazov IN, Moseenkov SI, IshchenkoAV, et al. 2012. CNT/PMMA electromagnetic coating: effect of carbon nanotube diameter. Fullerene, Nanotube. *Carbon Nanostruct*, vol. 20, issue 4-7, pp. 527–530.
13. Breuer O, Sundararaj U. 2004. Big returns from small fibers: a review of polymer/carbon nanotube composites. *Polym Compos*, vol. 25, issue 6, pp. 630–645.
14. Xu XJ, Thwe MM, Shearwood C, Liao K. 2001. Mechanical properties and interfacial characteristics of carbon-nanotube-reinforced epoxy thin films. *Appl Phys Lett*, vol. 81, issue 15.
15. Jin L, Bower R, Zhou O. 1998. Alignment of carbon nanotubes in a polymer matrix by mechanical stretching. *Appl Phys Lett*; vol. 73, issue 9.
16. Kanygin MA, Selyutin AG, Okotrub AV, Bulusheva LG. 2012. Anisotropic permittivity of multi-walled carbon nanotube/polystyrene composites. *Fullerene, Nanotube, Carbon Nanostruct*, vol. 20, issue 4-7, pp. 523–526.
17. Goh PS, Ismail AF, Ng BC. 2014. Directional alignment of carbon nanotubes in polymer matrices: contemporary approaches and future advances. *Composites*, vol. 56, pp. 103–126.
18. H.W. Kroto, J.R. Heath, S.C. O'Brien, R.F. Curl, R.E. Smalley. 1985. C_{60}: Buckminsterfullerene. *Nature,* vol. 318, pp. 162-163.
19. S. Iijima. 1991. Helical microtubules of graphitic carbon. *Nature*, vol. 354, pp. 56-58.
20. S. Iijima, and T. Ichihashi. 1993. Single-shell carbon nanotubes of 1-nm diameter. *Nature*, vol. 363, pp. 603-605.
21. J. Hone, I. Ellwood, M. Muno, A. Mizal, M.L. Cohen, A. Zettl, A.G. Rinzler, R.E. Smalley. 2005. Carbon Nanotube Based Composites- A Review. *Phys. Rev. Lett*, vol. 80, pp. 31-46.
22. E.N. Ganesh. 2013. Single Walled and Multi Walled Carbon Nanotube Structure, Synthesis and Applications. *IJITE*, vol. 2, issue 4, pp. 311-320.
23. Vimal Kumar Patel. 2009. [online document]. [Accessed 5.04. 2015]. Available at http://www.oocities.org/vimal_pro2/CNT.html

24. Jeroen W. G. Wilder, Liesbeth C. Venema, Andrew G. Rinzler, Richard E. Smalley, Cees Dekker. 1998. Electronic structure of atomically resolved carbon nanotubes. *Nature*, vol. 391, pp. 59-62.
25. Ph. Avouris, J. Appenzeller, R. Martel, and S. Wind. 2003. Carbon nanotube electronics. *IEEE***,** vol. 91, pp. 1772-1784.
26. Sander J. Tans, Alwin R. M. Verschueren, Cees Dekker. 1998. Room-temperature transistor based on a single carbon nanotube. *Nature*, vol. 393, pp. 49-52.
27. B.Q. Wei, R. Vajtai, P.M. Ajayan. 2001. Reliability and current carrying capacity of carbon nanotubes. *Appl. Phys. Lett*. vol. 79, issue 8, p. 1172.
28. D.H. Robertson, D.W. Brenner, J.W. Mintmire. 1992. Energetics of nanoscale graphitic tubules. *Phys. Rev.* B, vol. 45, issue 21, pp. 12592-12595.
29. M.F. Yu. 2000. Tensile loading of ropes of single wall carbon nanotubes and their mechanical properties. *Phys. Rev. Lett*, vol. 84, pp. 5552-5555.
30. B.I. Yakobson, C.J. Brabec, J. Bernholc. 1996. Nanomechanics of Carbon Tubes: Instabilities beyond Linear Response. *Phys. Rev. Lett*, vol. 76, issue 14, pp. 2511-2514.
31. J.Hone. 2001. Phonons and Thermal Properties of Carbon Nanotubes. *Applied Physics*, vol. 340, pp. 273-286.
32. W. Yi, L. Lu, D.L. Zhang, Z.W. Pan, S.S. Xie. 1999 Linear specific heat of carbon nanotubes. *Phys. Rev. B*, vol. 59**,** pp. 9015-9018.
33. A. Mizel, L.X. Benedict, M.L. Cohen, S.G. Louie, A. Zettl, N.K. Budraa, W.P. Beyermann. 1999. Analysis of the low-temperature specific heat of multiwalled carbon nanotubes and carbon nanotube ropes. *Phys. Rev. B*, vol. 60, p. 3264.
34. J. Hone, B. Batlogg, Z. Benes, A.T. Johnson, J.E. Fischer. 2000. Quantized phonon spectrum of single-wall carbon nanotubes. *Science*, vol. 289, pp. 1730-1733.
35. J.C. Lasjaunias, K. Biljakoviæ, Z. Benes, J.E. Fischer, P. Monceau. 2002. Low-temperature specific heat of single-wall carbon nanotubes. *Phys. Rev. B*, vol. 65, issue 11, p. 113409.
36. J. Hone, M. Whitney, C. Piskoti, A. Zettl. 1999. Thermal conductivity of single-walled carbon nanotubes. *Phys. Rev. B*, vol. 59, issue 4, pp. 2514-2516.
37. P. Kim, L. Shi, A. Majumdar, P.L. McEuen. 2001. Thermal Transport Measurements of Individual Multiwalled Nanotubes. *Phys. Rev. Lett*, vol. 87, issue 21, p. 215502.
38. L. X Benedict, S. G Louie, M.L. Cohen. 1996. Heat capacity of carbon nanotubes. *Solid State Comm*, vol. 100, pp. 177-180.
39. N. Popov. 2002. Low-temperature specific heat of nanotube systems. *Phys. Rev.* B, vol. 66, issue 15, p. 153408.

40. M. Tian, F. Li, L. Chen, Z. Mao. 1998. Carbon Nanotube Based Composites- A Review. *Phys. Rev. B*, vol. 58, p. 1166.
41. L. Grigorian, G.U. Sumanasekera, A.L. Loper, S.L. Fang, J.L. Allen, P.C. Eklund. 1999. Giant thermopower in carbon nanotubes: A one-dimensional Kondo system. *Phys. Rev. B*, vol. 60, issue 16, pp. 11309-11312.
42. M. Wilson et al. 2002. Nanotechnology: Basic Science and Emerging Technologies. Boca Ratón, EUA : Chapman and Hall.
43. NANOTECHNOLOGY. [online document]. [Accessed 6.04. 2015]. Available at http://www.gitam.edu/eresource/nano/nanotechnology/tem.htm
44. Polymer materials. Products, equipment, technology magazine. [online document]. [Accessed 10.04. 2015]. Available at http://www.polymerbranch.com/catalogp/view/5.html
45. O.V. Sedelnikova, M.A. Kanygin, E.Yu. Korovin, L.G. Bulusheva, V.I. Suslyaev b, A.V. Okotrub. 2014. Effect of fabrication method on the structure and electromagnetic response of carbon nanotube/polystyrene composites in low-frequency and K_a bands. *Composites Science and Technology*, vol. 102, pp. 59-64.
46. Binnig, G., Smith D. P. E. 1986. Single-tube three-dimensional scanner for scanning tunneling microscopy. *Review of Scientific Instruments*, vol. 57, issue 8, pp. 1688-1689.
47. Iakoubovski K. 2009. Techniques of aligning carbon nanotubes. *Cent Eur J Phys*, vol. 7, pp. 645–653.
48. Mike McElfresh. 1994. Fundamentals of magnetism and magnetic measurements featuring quantum design's magnetic property measurment system. Sorrento valley Rd San Diego: Quantum Design, Inc.
49. Cappella B, Dietler G. 1999. Force-distance curves by atomic force microscopy. *Surface Science Reports* , vol. 34, issue 1, pp. 1,5-3,104.
50. Binnig, G., Quate, C. F., Gerber, Ch. 1986. Atomic Force Microscope". *Physical Review Letters*, vol. 56, issue 9, pp. 930–933.
51. Mil Kapton® Tapes, RoHS Compliant [online document]. [Accessed 5.04. 2015]. Available at http://www.kaptontape.com/1_Mil_Kapton_Tapes.php